

Ti Passivation from a Dissipative Structure of the oxide layer

Authors: Weiwei Lao^{1†}, Qiaojie Luo^{1†}, Ying Huang^{2†}, Haixu Zhong³, Chaoqian Lou¹, Jiajia Xu¹, Xiufang Wen³, Xuliang Deng^{2*}, Xiaojun Li¹, Qianming Chen¹, Xiaodong Li^{1*}

Affiliations:

¹ School of Stomatology, Stomatology Hospital, Zhejiang University School of Medicine, Hangzhou 310006.

² National Engineering Laboratory for Digital and Material Technology of Stomatology, Beijing Laboratory of Biomedical Materials, Peking University School and Hospital of Stomatology, Beijing 100081, PR China.

³ School of Chemistry and Chemical Engineering, South China University of Technology, Guangzhou, 510640, China

* Corresponding author. Email: cisarli@zju.edu.cn; kqdengxuliang@bjmu.edu.cn.

† These authors contributed equally to this work.

Abstract:

For the long-standing riddle of metallic passivation, the second law of thermodynamics helps little. But this study shows that Ti passivation layer coming from room-temperature spontaneous oxidation possesses a dissipative structure which naturally extends from the lattice structure of Ti matrix. Macroscopically, its oxidation degree, oxygen content and amorphous structures exhibit a gradient decline from its surface to its bottom. Beneath a stable chemisorbed oxygen-metal atom monolayer, residue Ti lattice structures resemble stones and amorphous structures composed of TiO_2 , Ti_2O_3 and TiO resemble mortar, together they forming a heterogeneous stone-wall like structure. The rapid formation of the stable chemisorbed monolayer passivates the outmost Ti atoms to start Ti passivation, and subsequently a dissipative mechanism of oxidation cracks the Ti lattice structures and thus the oxide layer is formed and effect passivation. The solid phase formed by the open, stable, macroscopically-ordered, non-equilibrium oxide film, which can be aptly called “the dissipative oxidation phase”, theoretically does not end in complete oxidation of thermodynamic stability. This study derails both the adsorption theory of passivation and the theory of passivity film, and thus sheds new light on the metallic passivation.

Main Text:

For the last over 170 years, numerous explorations on the structure and formation kinetics and mechanism of metallic passivation, and the knowledge of passivation gained has driven the development of metal industries that underpinned the modern civilization^{1,2}. However, subject to the limitations of instruments, analysis methods, characterization and passivation theories, the structural features and working mechanisms of the passivation layer largely remain veiled^{3,4}.

First, the widely used electrochemical measurements have limitations involving its complicated detection environment, multiple factors with uncertain mechanism and unknown interactions that influence oxidation behaviors, implicating multiple components and complex structures of oxidation products. Together, they make it hard to investigate formation kinetics and structure of passivation film^{5,6}. Moreover, electrochemical analysis is a secondary analysis technique based on electrical signals and cannot directly characterize passivation film. Third, spectral characterizations, such as X-ray photoelectron spectroscopy (XPS)^{7,8}, X-ray absorption near edge structure (XANES)^{9,10} and extended X-ray absorption fine structure (EXAFS)^{11,12} reflect the average data of local domain information but fall short of the precise local structural characteristics. To make matter worse, two inherent features of the passivation film are ignored inadvertently. Despite all the attention paid to the disordered microstructure of this ultrathin film and its evolution, it is actually a tangible and measurable macroscopic system and its macroscopic structural features are ignored inadvertently. And during passivation a polycrystalline metal is of an open complex system. Actually, the second law of thermodynamics is of no avail here. Take a simple titanium (Ti) passivation layer by spontaneous oxidation at room temperature as an example. The finite spontaneous oxidation inputs oxygen to produce oxides and release reaction heat, thus dividing the open system into two subsystems, the oxide layer and the internal matrix. The non-equilibrium Ti oxide layer of insufficient oxidation can

stably protect its internal metal matrix from oxidation corrosion and remold its properties^{13,14}, while the complete oxidation of iron and other metals with thermodynamically stability as endpoint always results in metallic corrosion and failure of various applications¹⁵ costing trillions every year globally¹⁶.

Dissipative structure theory is useful to explain the structural evolution of an open, complex and macroscopic system from chaotic disorder to stable order far from equilibrium state^{17,18}. The theory teaches that for a system of dissipative structure, an ordered stable structure can be spontaneously formed in non-equilibrium state relying on a nonlinear interaction mechanism between different subsystems, an inherent feature. Meanwhile, by this nonlinear interaction mechanism which dissipates fluctuations in the open system caused by the environmental stimuli within a certain intensity range, the dissipative structure can keep stable.

Inspired by this theory, we propose that by active applying a single-factor environmental stimulus to cause fluctuations, in turn the traces left on the open system by the fluctuations may provide clues of its structural features and evolution mechanism. In this line, we design this study, namely a set of three kinds of gradient-upgrading oxidizing stimuli to treat fresh Ti discs at room temperature: NA-Ti group, treated under the atmospheric environment; O₃-Ti group, treated under the atmospheric environment which contains pumped O₃ (42.5±5.3mg/h); O-Ti group, treated under UV (188nm) irradiated atmospheric environment that includes UV-split O atoms and O₃ (44.4±3.9mg/h) formed via the combination of O atoms and O₂. The three oxidizing stimuli can drive the oxide layer to produce structural fluctuations dependent only on the oxidation potential of single factor. Through the comparative studies of components, structures and properties of the three spontaneously-formed oxide layers, we find that Ti passivation layer demonstrates a typical dissipative mechanism and possesses a dissipative structure.

The heterogeneous oxide layer organizes itself in gradient-order

Limited by the electron escape depth, the detection depth on Ti surface of XPS is about 2~3nm, the upper of the oxide layer. For NA-Ti groups, the ratio of $\text{Ti}^{\text{metallic}}/\text{Ti}^{4+}$ decreases by 3.7% in 96h, while 9.1% for O_3 -Ti and 12.0% for O-Ti (Fig. 1A and Extended Data Fig. 1). The oxidation degree shows the highest rise in O-Ti group and even under dark conditions (Extended Data Fig. 2). Even so, $\text{Ti}^{\text{metallic}}$ peaks assigned to Ti matrix still exist in the upper oxide layer of the O-Ti group. Thus, the stable heterogeneous oxide layers are far from equilibrium state.

The EDS mapping analysis reveals a well-defined structure with the O-rich layer. Following increasing oxidation potential of the three oxygen species, the oxide layers grow increasingly thickened. Meanwhile, the oxygen content shows the same tendency as featured by the increased atomic amount ratio of O/Ti from 1.29 of NA-Ti to 1.45 of O_3 -Ti and 1.56 of O-Ti (Fig. 1B). Represented as line profiles across the oxide interface zone, the contents of Ti and O demonstrates opposite gradient trends in the three oxide films (Fig. 1C).

There is a stable chemisorbed oxygen-metal atom monolayer

UPS detection information is more surface sensitive ($\sim 10\text{\AA}$). After 96 hours' treatment by O_3 or O atoms, values of work function (ϕ) are 4.67eV and 4.74eV respectively, which are higher than 4.36eV of NA-Ti and 4.33eV of cp Ti, while much lower than ϕ of TiO_2 5.58eV (Fig. 2A). While stronger oxidation by O_3 or O atoms enhances the valence electron stability of the oxide layer and reduces their electron transfer and oxidation rates, the two oxide layers are still apt to be further oxidized. This suggests that the surface of the oxide layer may be covered with a stable structure which is neither composed of Ti oxides nor Ti metal, but it can resist the oxidation even by O atoms, one of the strongest oxygens, and determine electron transfer and oxidation rates. There may persist a stable chemisorbed oxygen-metal atom monolayer during growth of continuous oxidation¹⁹. Calculated O atom adsorption stability on different crystal

planes of hcp Ti is further shown in Fig. 2B and Extended Data Fig. 3. In the view of energy, the chemisorbed O-Ti atom monolayer is more stable than TiO. Thus, this monolayer can preferentially form to passivate the surface metal atoms. It is the work function of the oxides underlies this stable monolayer that affects the oxide film further oxidation.

The oxide layer consists of amorphous oxides and residues Ti lattice structure

Aberration-Corrected TEM (ACTEM) reveals the thickness of oxide layer is 6.3 ± 0.2 nm of O₃-Ti and 7.1 ± 0.2 nm of O-Ti [Fig. 3B(a) and Fig. 3C(a)], thicker than 5.3 ± 0.5 nm of NA-Ti [Fig. 3A(a), Fig. 3B(a) and Fig. 3C(a)]. The oxide layers extend from the lattice structure of Ti matrix and consist of amorphous structures and nanoscale lattice structures. The amount and area of amorphous structures decrease from the surface to the bottom. After O₃ or O atoms treatment, the lattice structures become smaller but more while the amorphous structures get larger. Nevertheless, even in O-Ti group, the nanoscale lattice structures still exist in the outmost layer. Interestingly, fast Fourier transform (FFT) pattern of any region in the three oxide layers is almost the same as the lattice structure of Ti matrix [Fig. 3A(b), Fig. 3B(b) and Fig. 3C(b)]. Together with the Ti^{metallic} existence detected by XPS, these nanoscale lattice structures can be of the Ti lattice structure. It contradicts with the established belief that the nanocrystals in passivation films are oxides²⁰. Actually, in the previous numerous reports, definite existence of metallic elements in the passivation films is also found²¹⁻²⁵. In room temperature atmosphere, subject to unreachable energy barrier of the formation of oxide crystals and high stability of the Ti lattice structure, the minimum energy principle determines that inadequate oxidation driven by finite spontaneous oxidation potential is more likely to result in the residue of Ti lattice structures rather than the formation of oxide nanocrystals in the passivation film.

The Ti L2- and L3-edge EELS spectra are further tested, for the centers of the L3 and L2 peaks are chemically shifted to higher energy losses as the oxidation degree increases^{26,27}. As

shown in Fig. 3A(c), Fig. 3B(c) and Fig. 3C(c), four typical positions are selected, the outmost, the middle, the bottom of the oxide layer and the Ti matrix adjacent to the oxide layer.

Disappearance of the O signals at the Ti matrix adjacent to the oxide layer exhibits a definite existence of an oxide layer. From the outmost to the bottom, Ti L3 and L2 peaks are chemically shifted from higher energy losses to lower energy losses. These phenomena indicate a gradient decline of Ti oxidation degree from the outmost to the bottom of the oxide layers.

Moreover, compared to NA-Ti group, the L3, L2 peaks of the middle and the bottom shift towards those of the outmost layer in the O-Ti group or O₃-Ti group, and their peaks of the middle layer almost coincide with that of the outmost layer. Clearly, after the treatment by O₃ or O atoms, Ti atoms at the middle oxide layer shows a more similar chemical environment to those at the outmost layer suggesting the oxidation degree of the oxide layer is significantly increased. On the other hand, although XPS results exhibit the highest contents of Ti⁴⁺ in the three upper oxide layers, the characteristic four-peak of EELS spectra of Ti⁴⁺ was not found in the three groups. This shows no 3-D aggregate structure of TiO₂ in the oxide layer. Therefore, the three oxide layers consist of the amorphous oxides and the residue Ti lattice structures.

More micro-strains and O-vacancies in a more stable oxide layer

High-Resolution TEM (HRTEM) demonstrates that the numbers of edge dislocations from one-dimensional lattice fringe images on O₃-Ti and O-Ti are also much more than that on NA-Ti (Extended Data Fig. 4). This is consistent with the micro-strain ε value calculation in thin-film X-ray diffractometry (TF-XRD) that there are more micro-strains in the oxide layer after O₃ or O atoms treatment ($O-Ti|\varepsilon| > O_3-Ti|\varepsilon| > NA-Ti|\varepsilon|$) (Fig. 4a). As shown in Fig. 4b, all the three films perform n-type semiconducting behaviors. The donor density of oxygen vacancies shows a faster growth in O₃-Ti and O-Ti than NA-Ti and NA₀-Ti, while the donor density of electrochemical-induced passivation layer decreases with the increase of voltage²⁸. This

demonstrates that the behaviors of Ti spontaneous oxidation of single factor are different from that of electrochemical oxidation with uncertain mechanisms by multiple factors.

Electrochemical impedance spectroscopy (EIS) data indicates that O₃-Ti and O-Ti have better corrosion-resistance performances than NA-Ti, and O-Ti is better than O₃-Ti (Extended Data Fig. 5, Extended Data Table. 1 and Table. 2). It shows Ti oxide layer keeps its own stability by adapting to environmental oxidizing stimuli. Based on the simple equivalent circuit and the thickness of passivation film ($L_{ss}=1.5-10\text{nm}$), the electric field strength, E_0 , can be calculated about $2.2 \times 10^6 \text{ Vcm}^{-1}$, which agrees with the assumption of the high field strength $\sim 10^6-10^7 \text{ Vcm}^{-1}$ within the metal passivation film³.

The oxide layer possesses a dissipative structure

Following the gradient-upgrading oxidizing stimuli the structural evolution of the three films reveals that Ti oxide layer of a macroscopic system has a dissipative structure. Firstly, while the Ti oxide layer gives Ti metal extraordinary stability, it consisting of amorphous oxides and residue lattice structure of Ti matrix is far from equilibrium state. Secondly, the finite spontaneous oxidation produces multiple oxides with microscopically disordered structures. However, as a macroscopic system, from the surface to the bottom Ti oxidation degree, oxygen content and amorphous structures tell a typical orderly structural feature of gradient decline. Thirdly, and more importantly, between the two subsystems--the oxide layer and the internal matrix, there exists a typical nonlinear interaction mechanism. Relying on it this passivation oxide layer is spontaneously formed via self-organization. The stronger structural fluctuations caused by O₃ or O atoms is restricted to the oxide layer beyond the internal matrix, as manifested by the fact that the oxide layer converts itself into a thicker, more oxygenated, more oxidized and stable oxide layer so as to be adaptive to the environmental stimuli through this nonlinear mechanism.

Microscopically, beneath the stable chemisorbed oxygen-Ti atom monolayer, as HRTEM shows (Extended Data Fig. 6), with the residue Ti lattice structures acting like stones and the amorphous oxides mortar, the spontaneous oxidation produces an oxide layer of a stone-wall like structure. This structure can make low the stress and strain energy caused by misfit between the residual lattice structures and the amorphous oxides^{29,30}, and thus stabilize the oxide layer. Moreover, following upgrading oxidizing stimuli, the amorphous structures increase while the residue lattice structures get smaller but more.

This characteristic-local structural evolution tells a unique dissipative mechanism of oxidation (Fig. 4c). There exists a specific surface area-large interface between the numerous residue lattice structures and the amorphous structures. In their interface, the micro-strains and O-vacancies are rich. Like chloride ion diffusion channels³¹, the interface regions may provide favorable channels for O^{2-} diffusion. Thus, under the stimuli of O atoms or O_3 , through these channels, higher oxidation potential can crack the residue lattice structures into smaller but more lattice structures, while make the amorphous regions bigger and more oxidized and even invade the matrix deeper. This thickens the oxide layer, enlarges the interface regions, and in turn increases the micro-strains and O-vacancies. A thicker, more oxygenated, higher oxidation and more stable film which is still in non-equilibrium state is achieved. It is clear that the oxidation cracking of the residue lattice structures, as a dissipative mechanism, dissipates the fluctuations caused by the environmental stimuli to keep the oxide film and the entire open system stable.

The simple passivation model, as shown in this study, sheds fresh light on general understanding of the passivation film. The two Ti surfaces by UV irradiation (254nm or 365nm) are also of a dissipative structure (Extended Data Fig. 7- Fig. 11). In the literature, although the environmental factors or investigation instruments and methods or material systems are different³²⁻³⁴, as open macroscopic systems, all these passivation films have the three typical

features of a dissipative structure: stable but in non-equilibrium state, gradient-ordered structure of the metallic oxidation degree and oxygen content, and a nonlinear interaction mechanism to dissipate the fluctuations caused by the environmental stimuli within a certain intensity range to keep the passivation films stable.

In derailing the adsorption theory of passivation⁴ and the theory of passivity film^{35,36}, this study reveals a new passivation mechanism of dissipation: the rapid formation of the stable chemisorbed monolayer passivates the outmost Ti atoms to start metallic passivation, and the oxide layer is subsequently formed and effects metallic passivation through the dissipative mechanism of oxidation cracking. The oxide film thus acting like a strong damper of oxidation keeps its own stability by adapting to external oxidizing stimuli. This film, however, is far from the complete oxidation of thermodynamical stability. It keeps being slowly oxidized over time even in the mild oxygen environments^{37,38}. The whole film is of a stable, ordered, open, non-equilibrium, solid phase spontaneously formed in a finite oxidation environment, where its state theoretically does not end in thermodynamic stability. This can be aptly called “the dissipative oxidation phase” and serve as a fresh ground for grasping metallic passivation.

Our findings exhibit the fundamental difference between Ti surface and surfaces of TiO₂ including amorphous or rutile or anatase. It refutes the misbelief that the properties of TiO₂ can explain the surface or interface phenomena of Ti metal³⁹⁻⁴¹. It also brings about insight to understand Ti related properties, e.g., the osseointegration mechanism of Ti implants. Once a Ti-based implant is inserted into the bone, a local acute inflammatory response immediately produces numerous reactive oxygen species (ROS)^{42,43}. The oxide film of dissipative structure can rapidly capture ROS in the surrounding environment. This not only lowers the ROS concentration, but also makes this film more stable, more corrosion resistant and even more hydrophilic, being of better bio-and histocompatibility. The positive-feedback mechanisms

between ROS and Ti passivation film can start subsequent cascaded biological events, leading to the final implant-bone osseointegration.

Our findings also deepen understanding of the acquisition of ultra-high vacuum by using Ti as gettering materials⁴⁴. The gettering properties of the evaporated Ti film have a clear dependence on the ionization (atomization) of the residual gas by a Penning gauge. L. Holland once proposed that there was no evidence that passivation films on metals grew faster in the presence of active oxygen, but penetration of a metal film by gas atoms so that the crystallites were oxidized on many sides would explain this phenomenon⁴⁵. This study shows that once O₂ is ionized into O atoms, within the same time span the evaporated Ti film is able to rapidly sorb more oxygen to produce a more stable oxide layer which has higher oxidation degree, more oxygen content and larger thickness. For this reason, a higher vacuum can be produced.

While the dynamics of passivation calls for further exploration, we show a new passivation mechanism of dissipation and thus propose that the metallic passivation can come from the formation of passivation film of a dissipative structure. These new ideas for metallic passivation theory will help much in fighting metal corrosion and protection. Moreover, our findings provide new evidence and impetus for the theory of dissipative structure and synergetics. For every matter individual and every form of life have the structural basis of self-becoming, self-protection and channels of exchange with external environment for matter and energy, the formation of macroscopically-ordered dissipative surfaces via self-organization might well be a common phenomenon. As a result, our findings and theory might contribute to general understanding of nature and science.

References

1. Macdonald, D. D. Passivity-the key to our metals-based civilization. *Pure Appl Chem.* **71**, 951-978 (1999).
2. Xu, H. S., Wang L., Sun D. B., Yu, H. Y. The passive oxide films growth on 316L stainless steel in borate buffer solution measured by real-time spectroscopic ellipsometry. *Appl Surf Sci.* **351**, 367-373 (2015).
3. Cabrera, N., Mott, N. F. Theory of the oxidation of metals. *Rep Prog Phys.* **12**, 163-184 (1948).
4. Uhlig H. H. The adsorption theory of passivity and the flade potential. *Z Elektrochem.* **62**, 626-632 (1958).
5. Ohtsuka, T., Nishikata A., Sakairi, M., Fushimi, K. *Electrochemistry for corrosion fundamentals* (Springer Singapore, Singapore, 2018).
6. Frankel, G. S. *Active Protective Coatings: New-Generation Coatings for Metals* (Springer Netherlands, Dordrecht, 2016).
7. Vogel, U. et al. Evaluation of a mobile vacuum transfer system for in vacuo XPS analysis using as-deposited Ti thin-films. *Vacuum.* **117**, 81-84 (2015).
8. Milošev, I., Metikoš-Huković, M., Strehblow, H. H. Passive film on orthopaedic TiAlV alloy formed in physiological solution investigated by X-ray photoelectron spectroscopy. *Biomaterials.* **21**, 2103-2113 (2000).
9. Wang, L. et al. Local fine structural insight into mechanism of electrochemical passivation of titanium. *Acs Appl Mater Inter.* **8**, 18608-18619 (2016).
10. Virtanen, S., Schmuki, P., Isaacs, H. S. In situ X-ray absorption near edge structure studies of mechanisms of passivity. *Electrochim Acta.* **47**, 3117-3125 (2002).

11. Wang, L. et al. In-situ XAFS and SERS study of self-healing of passive film on Ti in Hank's physiological solution. *Appl Surf Sci.* **496**, 143657 (2019).
12. Anspoks, A., Kalinko, A., Kalendarev, R., Kuzmin, A. Atomic structure relaxation in nanocrystalline NiO studied by EXAFS spectroscopy: Role of nickel vacancies. *Phys Rev B.* **86**, 174114 (2012).
13. Kasemo, B. Biocompatibility of titanium implants-surface science aspects. *J Prosthet Dent.* **49**, 832-837 (1983).
14. Lütjering, G., Williams, J. C. *Titanium* (Springer-Verlag, Berlin, ed. 2, 2007).
15. Newman, R. C., Sieradzki, K. Metallic Corrosion. *Science.* **263**, 1708-1709 (1994).
16. Koch, G. In *Trends in Oil and Gas Corrosion Research and Technologies* (Woodhead Publishing, Boston, 2017), pp. 3-30.
17. Prigogine, I. *From Being to Becoming* (W. H. Freeman & Co, San Francisco, 1980).
18. Prigogine, I. Time, Structure, and Fluctuations. *Science.* **201**, 777-785 (1978).
19. Uhlig, H. H. Structure and growth of thin films on metals exposed to oxygen. *Corros Sci.* **7**, 325-339 (1967).
20. Zhang, B. W. Passivation of nickel nanoneedles in aqueous solutions. *J Phys Chem C.* **118**, 9073-9077 (2014).
21. Lausmaa, J., Kasemo, B., Mattsson, H. Surface spectroscopic characterization of titanium implant materials. *Appl Surf Sci.* **44**, 133-146 (1990).
22. Binon, P. P., Weir, D. J., Marshall, S. J. Surface analysis of an original Brånemark implant and three related clones. *Int J Oral Max Impl.* **7**, 168-175 (1992).
23. Olefjord, I., Hansson, S. Surface analysis of four dental implant systems. *Int J Oral Max Impl.* **8**, 32-40 (1993).

24. Lynch, B., Wiame, F., Maurice, V., Marcus, P. XPS study of oxide nucleation and growth mechanisms on a model FeCrNiMo stainless steel surface. *Appl Surf Sci.* **575**, 151681 (2022).
25. Lin, T. C., Seshadri, G., Kelber, J. A. A consistent method for quantitative XPS peak analysis of thin oxide films on clean polycrystalline iron surfaces. *Appl Surf Sci.* **119**, 83-92 (1997).
26. Kourkoutis, L. F. et al. Atomic-resolution spectroscopic imaging of oxide interfaces. *Philos Mag.* **90**, 4731-4749 (2010).
27. Kim J. S. et al. Nanoscale bonding between human bone and titanium surfaces: osseohybridization. *Biomed Res Int.* **2015**, 960410 (2015).
28. Wang, L. et al. Quantitative analysis of local fine structure on diffusion of point defects in passive film on Ti. *Electrochim Acta.* **314**, 161-172 (2019).
29. Frank, F. C., Vandermerwe, J. H. One-dimensional dislocations. I. Static theory. *Proc R Soc Lon Ser-A.* **198**, 205-216 (1949).
30. Frank, F. C., Vandermerwe, J. H. One-dimensional dislocations. II. Misfitting monolayers and oriented overgrowth. *Proc R Soc Lon Ser-A.* **198**, 216-225 (1949).
31. Zhang, B. et al. Unmasking chloride attack on the passive film of metals. *Nat Commun.* **9**, 2559 (2018).
32. Lv, J. L., Liang, T. X., Wang, C., Dong, L. M. Surface corrosion enhancement of passive films on NiTi shape memory alloy in different solutions. *Mat Sci Eng C-Mater.* **63**, 192-197 (2016).
33. Noh, J. S., Laycock, N. J., Gao, W., Wells, D. B. Effects of nitric acid passivation on the pitting resistance of 316 stainless steel. *Corros Sci.* **42**, 2069-2084 (2000).

34. Li, D. G., Wang, J. D., Chen, D. R., Liang, P. Influence of passive potential on the electronic property of the passive film formed on Ti in 0.1 M HCl solution during ultrasonic cavitation. *Ultrason Sonochem.* **29**, 48-54 (2016).
35. Evans, U. R. CXL.-The passivity of metals. Part I. The isolation of the protective film. *J Chem Soc.* 1020-1040 (1927).
36. Evans, U. R. Inhibition, passivity and resistance: a review of acceptable mechanisms. *Electrochimica Acta*, **16**, 1825-1840 (1971).
37. Luo, Q. J. et al. Topography-dependent antibacterial, osteogenic and anti-aging properties of pure titanium. *J Mater Chem B.* **3**, 784-795 (2015).
38. Sundgren, J. E., Bodo, P., Lundstrom, I. Auger-electron spectroscopic studies of the interface between human-tissue and implants of titanium and stainless-steel. *J Colloid Interf Sci.* **110**, 9-20 (1986).
39. Aita, H. et al. The effect of ultraviolet functionalization of titanium on integration with bone. *Biomaterials.* **30**, 1015-1025 (2009).
40. Shah, F. A., Thomsen, P., Palmquist, A. Osseointegration and current interpretations of the bone-implant interface. *Acta Biomaterialia.* **84**, 1-15 (2019).
41. Prestat, M., Thierry, D. Corrosion of titanium under simulated inflammation conditions: clinical context and in vitro investigations. *Acta Biomaterialia.* **136**, 72-87 (2021).
42. Dziubla, T., Butterfield, D. A. *Oxidative Stress and Biomaterials* (Academic Press, London, 2016).
43. Nel, A., Xia, T., Mädler, L., Li, N. Toxic potential of materials at the nanolevel. *Science.* **311**, 622-627 (2006).
44. Stow, R. L. Titanium as a gettering material. *Nature.* **184**, 542-543 (1959).
45. Holland, L. Sorption of activated gases by titanium films. *Nature.* **185**, 911-912 (1960).

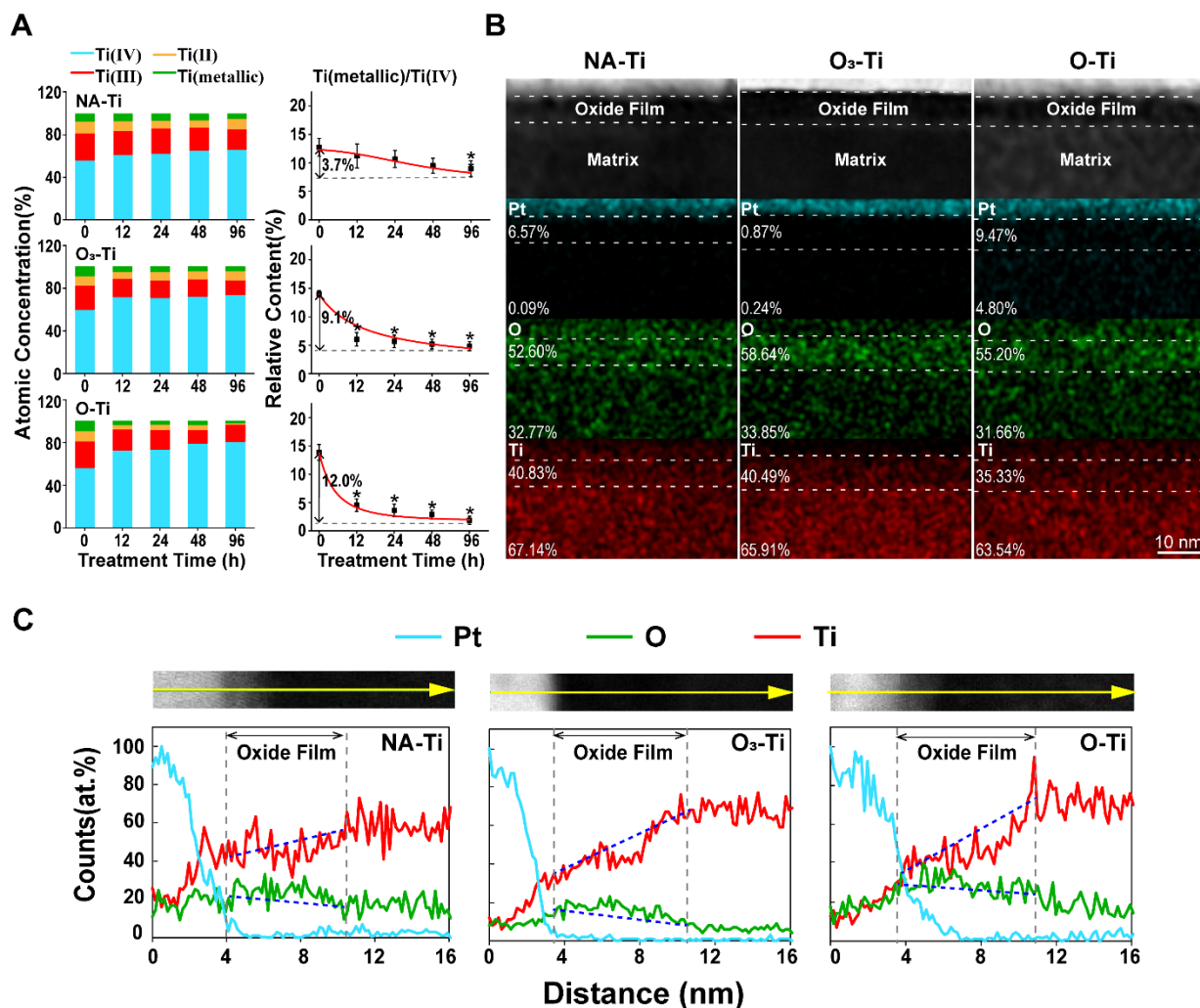


Fig. 1. Heterogeneous Ti oxide layer in a gradient-order state. (A) Elemental analysis of XPS spectra on surfaces of NA-Ti, O₃-Ti and O-Ti. Left: content percentage of various Ti valence states; Right: trend charts of $\text{Ti}^{\text{metallic}}/\text{Ti}^{4+}$ relative content. * $p < 0.05$ vs. treatment time of 0h in the same group. (B) Super-X EDS mapping and (C) line profiles of Ti oxide films on NA-Ti, O₃-Ti and O-Ti with treatment for 48h.

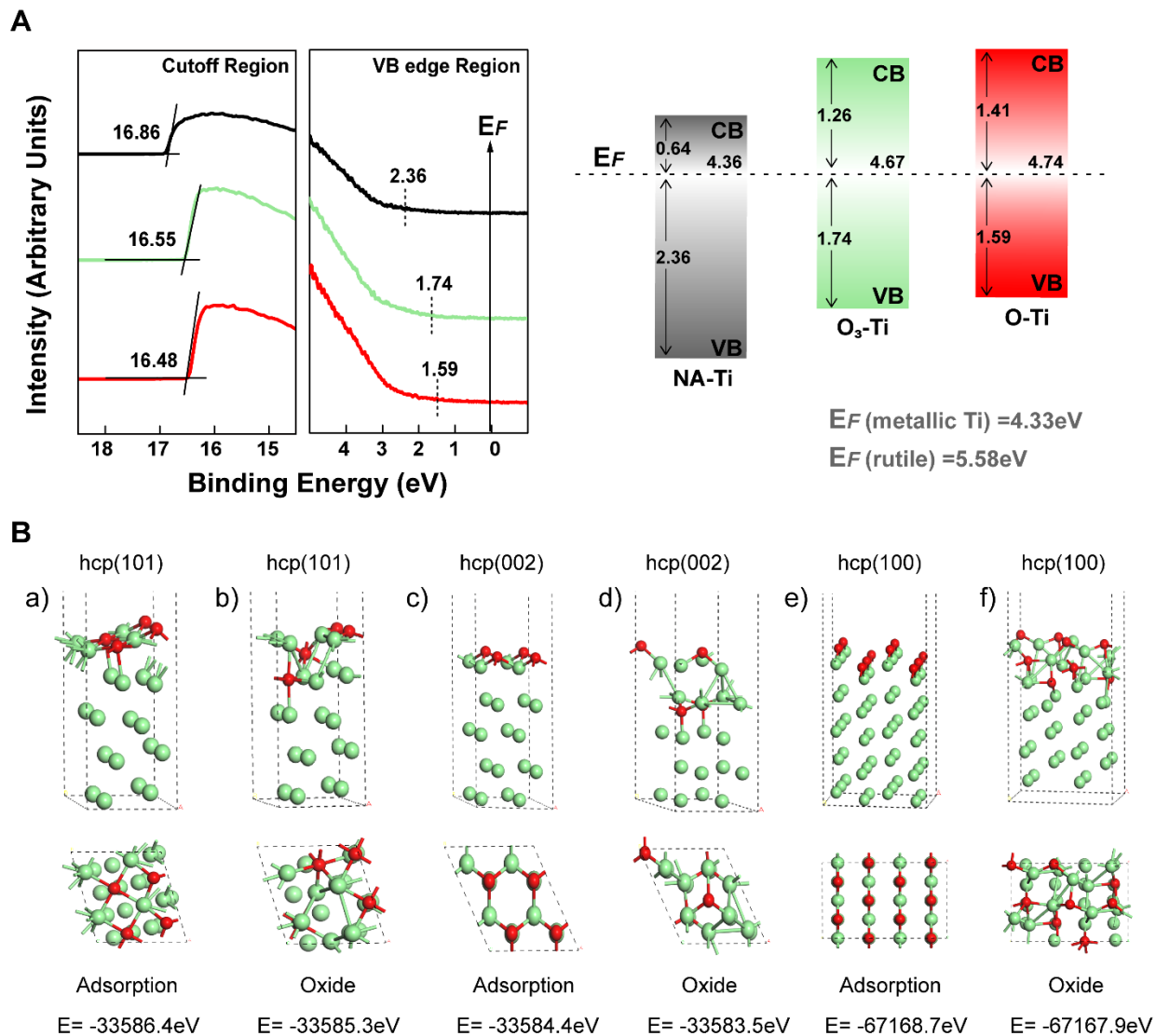


Fig. 2. A stable chemisorbed O-Ti atom monolayer on the outmost Ti surface. (A) UPS spectra of the cutoff region and VB edge region for different Ti oxide films. Spectra from bottom to top represent oxide films of O-Ti, O_3 -Ti and NA-Ti with treatment for 96h. Right three columns represent correlative UPS measured energetic levels. E_F , CB, and VB represent Fermi level, conductive band and valence band, respectively. (B) Side view and top view of adsorption models of O atoms on hcp Ti (101) surface in a), (002) surface in c) and (100) surface in e). Side view and top view of Ti-O oxide models on hcp Ti (101) surface in b), (002) surface in d) and (100) surface in f). The simulated system has better stability with larger absolute value of energy (E). Take the

energy at infinity from the nucleus as zero.

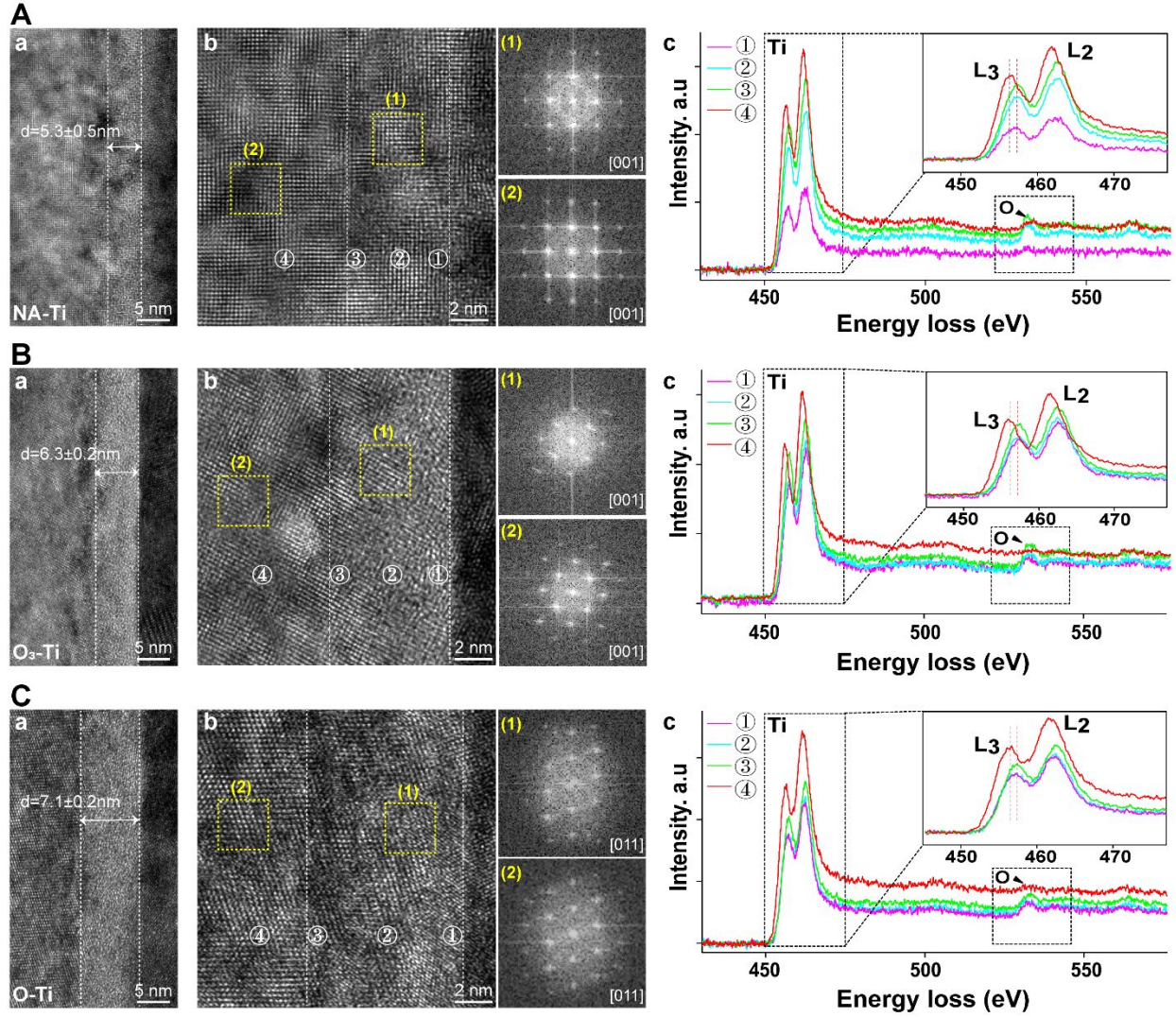


Fig. 3. Cross-sectional HRTEM images and EELS analysis of the three Ti oxide layers. The oxide layers on O-Ti and O₃-Ti are thicker than that on NA-Ti with treatment for 48h [A(a), B(a) and C(a)]. Fast Fourier transform (FFT) patterns of selected regions in the oxide layer (1) are almost the same as that of Ti matrix (2) in each group [A(b), B(b) and C(b)]. EELS analysis is performed on NA-Ti, O₃-Ti and O-Ti with treatment for 48h [A(c), B(c) and C(c)]. Numbers in left HAADF-STEM image: ①-the surface of the oxide layer; ②-the middle of the oxide layer; ③-the bottom of the oxide layer; ④-the metal matrix of the oxide layer. There are two

characteristic peaks of Ti signals and significant O signals (main adsorbed species in our experiments; Ti L2,3-edge: 462eV&456eV and O K-edge: 532eV) in three different EELS results presented. The centers of the L3 and L2 peaks are chemically shifted to higher energy losses as the degree of oxidation increased.

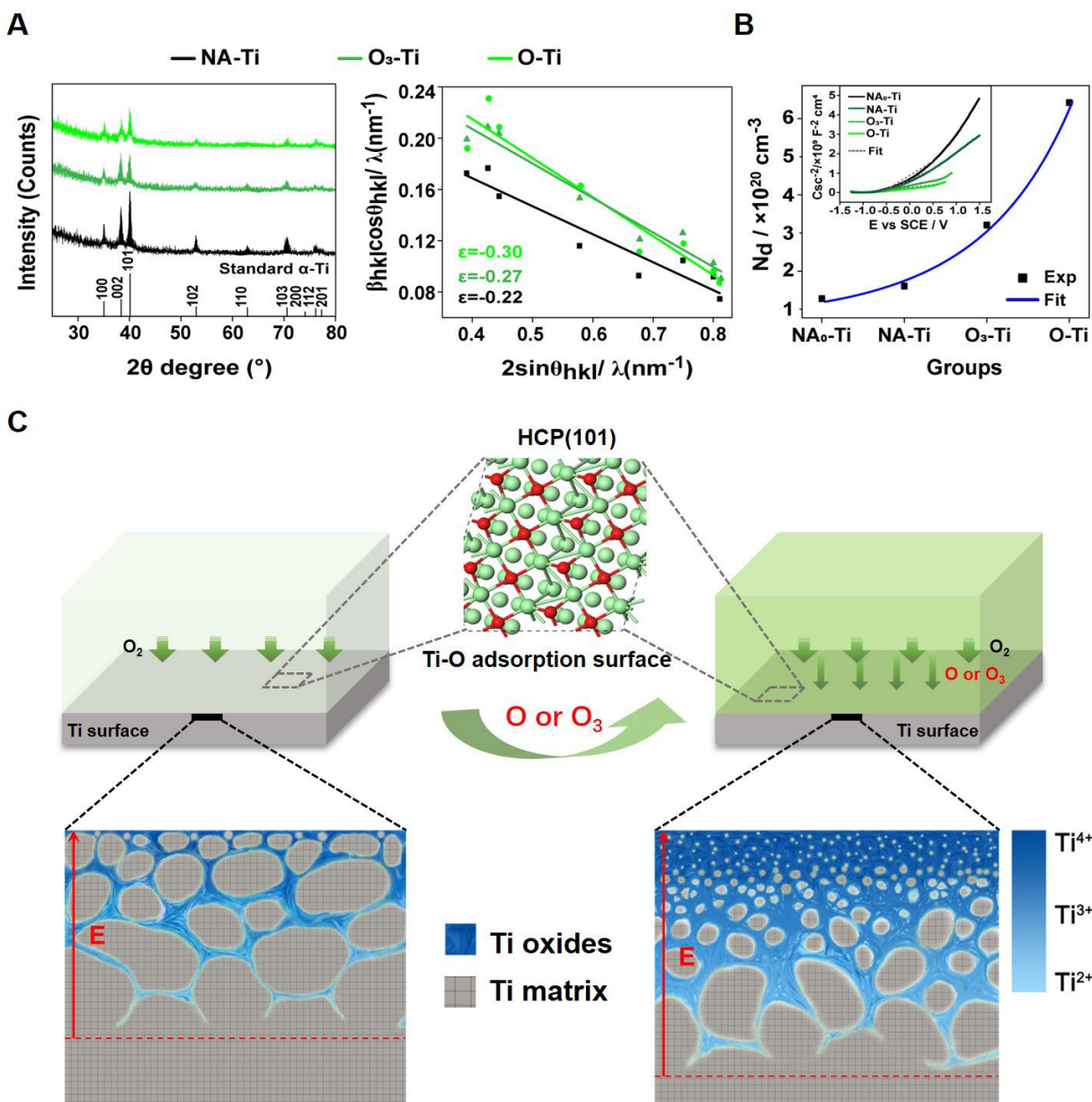


Fig. 4. Micro-strains and O-vacancies analysis of the three Ti oxide layers and schematic illustration of the dissipative structure of Ti passivation film. (A) The micro-strain ϵ of each corresponding Williamson-Hall (WH) plot (right) from TF-XRD results (left) showed that there

are more structural defects in oxide layers of O-Ti and O₃-Ti than NA-Ti with treatment for 48h. (B) Potential dependence of donor density calculated from Mott-Schottky plots (inset) of Ti passivation films of NA₀-Ti (tested immediately) and NA-Ti, O₃-Ti, O-Ti (tested after treatment for 48h). Lines are fitted curves given by the equation (7) in Methods. (C) Microscopically, beneath a stable chemisorbed O-Ti atom monolayer, with the residue Ti lattice structures like stones, the amorphous oxides mortar, the spontaneous oxidation produces a stable stone-wall like oxide layer. By a dissipative mechanism of oxidation cracking of the residue lattice structures, this oxide layer is adaptive in protecting the internal matrix from environmental oxidation stimuli.

Methods

Samples treatment with three oxidizing environments

Ti discs (10 mm in diameter, 1 mm in thickness) and Ti plates (size of 10 mm × 20 mm × 1mm) were prepared by machining commercial pure Ti materials (Grade I). Ground and mechanochemical polished to 100 Å roughness. Polished samples were then successively ultrasonically cleaned with acetone, ethanol and deionized water, and dried with nitrogen. All discs were treated under three kinds of gradient-upgrading oxidizing environments, (1) NA-Ti group, treated under the atmospheric environment; (2) O₃-Ti group, treated under the atmospheric environment which contains pumped O₃ (42.5±5.3mg/h); (3) O-Ti group, treated under UV irradiated atmospheric environment that includes UV-split O atoms and O₃ (44.4±3.9mg/h) formed via the combination of O atoms and O₂ (formulas 1 and 2). The wavelengths of UV irradiation were 253.7nm (100%) and 184.9nm (19%) respectively, which were performed with two 8W bactericidal lamps (Cnlight, Guangdong, China) for different times in an ultraviolet disinfection cabinet with volume of 40cm*30cm*25cm.

According to the Chapman Mechanism, when the UV wavelength is below 242nm, following reactions occur in air:



Herein, $h\nu$ is the UV photon and [O] is a free oxygen atom.

Chemical composition measurements by X-ray photoelectron spectroscopy

The chemical composition of the surfaces was evaluated by X-ray photoelectron spectroscopy (AXIS Supra, Kratos, UK) with *Al Kα* monochromatic X-ray source ($h\nu = 1486.6 \text{ eV}$) under high vacuum conditions. Relative concentrations of the detected elements were calculated by taking the percentages of their peak-to-peak heights in differentiated survey

spectra, and after correction by atomic sensitivity factors.

Ultra-violet photoelectron spectroscopy study

Ultra-violet photoelectron spectroscopy (UPS) with a pass energy of 1 eV, a target current of 50 mA was used to calculate the work function of the materials. Here, He I (21eV) was used to turn on the UV source. Work function (ϕ) is a parameter signifying the electronic stability of the crystallographic structure and its theoretical formula is:

$$\phi = E_e - E_F \quad (3)$$

Herein, E_e is the potential energy of electrons outside the surface of Ti passivation film and E_F the Fermi energy level of the solid material. Generally, the potential of electrons on the vacuum side outside the material surface is selected as the reference zero point, that is, the vacuum energy level is set as $E_{vac} = 0$, and $E_e = E_{vac} = 0$. Therefore, the above formula is:

$$\phi = -E_F \quad (4)$$

Computational methods and models

The adsorption models of O atoms on different crystal faces of hcp Ti as well as oxide models of TiO were constructed respectively.

The Density functional theory (DFT) calculations of adsorption in models were conducted using the Cambridge Sequential Total Energy Package (CASTEP) computer code. The Perdew-Burke-Ernzerhof functional within the generalized gradient approximation (GGA-PBE) was generally regarded as the most appropriate for the investigation of molecular adsorbate systems and applied to acquire the electronic energies⁴⁶. The cutoff energy of kinetic energy was set to 571.4eV and the width of smearing was set to 0.1eV with $4 \times 4 \times 1$ mesh of k-points. Meanwhile, 5-layer slabs of Ti atoms were built, and all crystal surfaces of hcp Ti were used to establish the p (2×2) supercell. There was a 15 Å vacuum slab to avoid the interaction between periodically repeated slabs^{47,48}.

TEM specimen preparation and technology

The cross-sectional TEM specimen (10 μ m in width) was prepared by an FEI Quanta 3D FEG in combination with focused ion beam (FIB)/SEM workstation with 5kV working voltage of the electron beam and 2-30kV voltage of ion beam. As a result, we obtained a distinct metal/oxide film interface and characterize the structure of the interface region. During sample preparation and subsequent TEM observation, the thin passivation film was strictly ensured free of mechanical and beam-induced damage.

TEM observation

The HRTEM and HAADF-STEM images were obtained by aberration-corrected transmission electron microscopy (Titan G² 80-200 ChemiSTEM, FEI, USA) at a working voltage of 200kV in order to observe micro morphologies and phase structures. Selected area electron diffraction (SAED) was used to certify crystal structures of the passivation film and its adjacent areas. We also used the advanced Super-X EDS system with four detectors for the mapping and line scan analysis to evaluate element contents in different depths of the passivation film, which significantly shortened the experimental span and thus effectively avoided beam damages to specimens. The Electron energy loss spectroscopy (EELS) analysis was performed in a FEI Titan G² 80-200 ChemiSTEM operated at 200kV with a nominal energy resolution of 1.1eV. Under the STEM mode, the convergence angle was 21.4mrad and the collection angle was 38.07mrad. EELS data were only smoothed after deducting the background.

Chemical phase detection by thin film X-ray diffraction

The phase composition was studied by thin film X-ray diffraction (XRD) using an X-ray diffractometer (D8 DISCOVER, Bruker, Germany) with Cu Ka1 (λ = 1.540598 Å)/Ka2 (λ =1.544426 Å) radiation with a ratio of 0.5, operating at 40 kV and 25 mA with a scan step size of 0.0167113° between 5° and 80° of measured scan.

After measuring the diffraction pattern, the Williamson Hall (WH) method was used for further analysis. In WH plots, the full width at half maximum (FWHM) is plotted relative to the diffraction angle for each diffraction peak. This method is the basic approach to evaluate the micro-strain ε that is produced by dislocations⁴⁹. When X-rays with a wave length λ are used for diffraction analysis and a diffraction angle θ and FWHM β is obtained in each diffraction peak, the following Williamson-Hall (WH) equation is constructed as follows:

$$\frac{\beta \cos \theta}{\lambda} = \alpha + \frac{\varepsilon \cdot 2 \sin \theta}{\lambda} \quad (5)$$

Here, the parameter α is dependent on the crystallite size. In poly crystalline titanium metals, several diffraction peaks appear and $\frac{\beta \cos \theta}{\lambda}$ and $\frac{2 \sin \theta}{\lambda}$ are obtained from each diffraction peak. Therefore, the values of parameter α and ε are determined based on the relation between $\frac{\beta \cos \theta}{\lambda}$ and $\frac{2 \sin \theta}{\lambda}$. We further calculated $\frac{\beta \cos \theta}{\lambda}$ and $\frac{2 \sin \theta}{\lambda}$ from every diffraction peak of tested XRD curves and made a linear fit of them. The slope of each curve represents the average micro-strain ε of each Ti surface.

Electrochemical measurements

Ti samples in size of 10 mm × 20 mm × 1mm were used for electrochemical measurements. A classical three-electrode cell with titanium plate as study electrode, a Pt wire as counter electrode and Ag/AgCl as reference electrode was connected to a CS310H electrochemical workstation (Wuhan Corrtest Instruments Corp., Ltd., CHN), and a computer with CS Studio5 software was used for all the electrochemical measurements. A PBS (NaCl: 145mM, Na₂HPO₄·12H₂O: 8.1mM, NaH₂PO₄·2H₂O: 1.9mM) solution with pH 7.2-7.4 was used as electrolyte. The analyzed area immersed in electrolyte was 10 mm×10 mm of the titanium surface. All potential data in the following are refer to Ag/AgCl electrode and all electrochemical measurements were carried out at 37±1°C temperature. The open circuit potential (OCP)

measurement was carried out for 30 min starting from the electrode immersing into the electrolyte. The electrochemical impedance spectroscopy (EIS) measurements were carried out under potentiostatic condition at OCP with 10mV amplitude AC voltage signal, and the applied frequency range was from 10^5 Hz down to 10^{-2} Hz. The impedance data was analyzed using ZSimpWin 3.0 software. The potentiodynamic polarization curves were obtained in the range of $OCP \pm 0.5V$ using a scan rate of 1 mV/s. The corrosion potential (E_{corr}) and corrosion current density (I_{corr}) were determined by Tafel slope extrapolation. All electrochemical tests were repeated three times to ensure reproducibility and statistically analyzed to gain the standard deviations.

The electric field strength of passivation film, E_0 , can be calculated from the following equation²⁰:

$$L_{ss} = \frac{1}{E_0}(1 - \alpha)E + B \quad (6)$$

where E is the film formation potential measured as 0.08V-0.10V in tafel curves, α represents the polarizability of the film reported as 0.8, B is a constant related to the film thickness at 0V.

Differential capacitance measurements

Mott-Schottky experiments were conducted to study the semiconducting type and dopant density of the passive film and were performed at a constant frequency of 1 kHz with an amplitude signal of 5mV. The spectra were gotten by sweeping scan of $OCP \pm 1.0 V$ at a rate of 20 mV s⁻¹. At high frequency, the space charge capacitance was calculated assuming $C_{sc} = (-Z_{im}2\pi f)^{-1}$, where f was the frequency and Z_{im} was the imaginary component of impedance. The density of donors can be calculated using the Mott-Schottky relationship, as given by the following equation²⁰:

$$\frac{1}{C_{sc}^2} = \frac{2}{\epsilon_r \epsilon_0 N_d A^2} (E - E_{fb} - \frac{kT}{e}) \quad (7)$$

where N_d is the donor density, ϵ_r is the relative dielectric constant, ϵ_0 is the vacuum dielectric constant, A is the sample contact area, E_{fb} is the flat band potential, e is the electron charge, k is the Boltzmann constant, and T is the temperature in Kelvin.

Influence of UV irradiation on the structure and properties of Ti passivation film

It should be noted that in addition to UV wavelength of 184.9nm, UV lamps used in this study contains UV wavelength of 254nm. To explore the influence of UV irradiation on the passivation film, we also applied two other types of UV irradiations in this work, with central wavelengths of 254nm or 365nm respectively, to treat Ti discs. Indeed, both UV irradiations have little effect on the structure and properties of Ti passivation film, slightly stronger than NA-Ti group and much weaker than O₃-Ti and O-Ti. The influence of UV2 irradiation seems stronger than that of UV3 irradiation (Extended Data Fig. 7- Fig. 11, Extended Data Table. 1 and Table. 2). The reason might be resulted from UV-induced effect of Ti passivation film, which needs to be further studied.

Statistical analysis

Relative contents of elements from XPS data in accordance with normal distribution and homogeneity (Shapiro–Wilk Test, $p > 0.05$ & Levene Test, $p > 0.05$) were compared by two-way ANOVA test followed by Tukey’s Post hoc test. All data are shown as mean \pm standard deviation (SD) and have been tested using SPSS statistical software (V20, SPSS, Inc., USA). The statistical significance (p value) was set at a level of $p=0.05$.

References

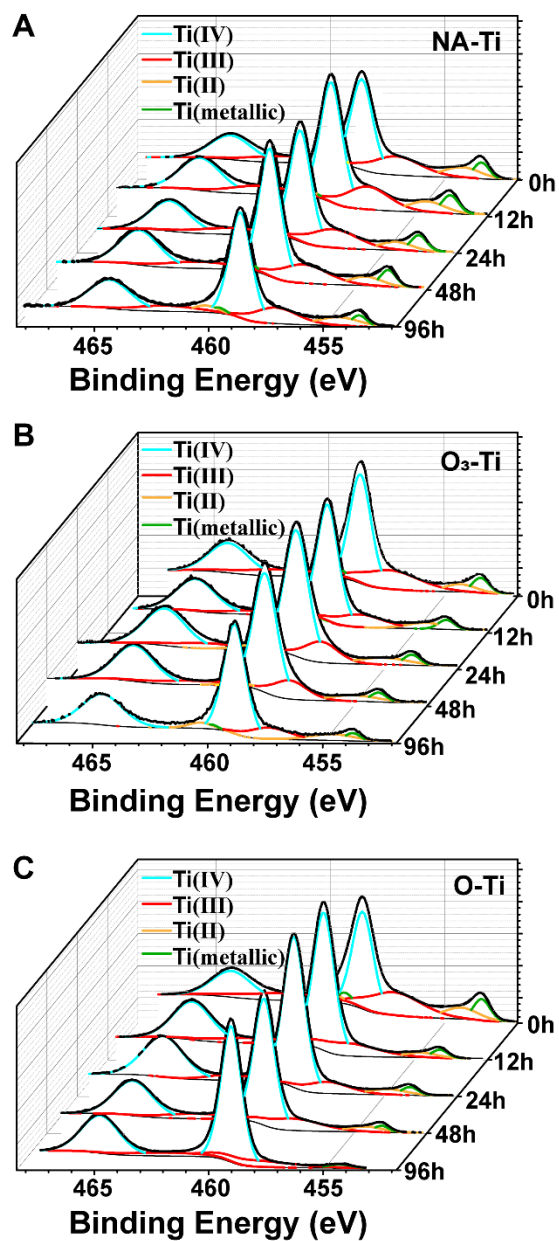
46. Perdew, J. P., Burke, K., Ernzerhof, M. Generalized gradient approximation made simple. *Phys Rev Lett.* **77**, 3865-3868 (1996).

47. Harrison, M. J., Woodruff, D. P., Robinson, J. Density functional theory investigation of the structure of SO₂ and SO₃ on Cu (111) and Ni (111). *Surface Science*. **600**, 1827-1836 (2006).
48. Ren, L. et al. DFT studies of adsorption properties and bond strengths of H₂S, HCN and NH₃ on Fe (100). *Appl Surf Sci*. **500**, (2020).
49. Pelleg, J., Elish, E., Mogilyanski, D. Evaluation of average domain size and microstrain in a silicide film by the Williamson-Hall method. *Metall Mater Trans A*. **36**, 3187-3194 (2005).

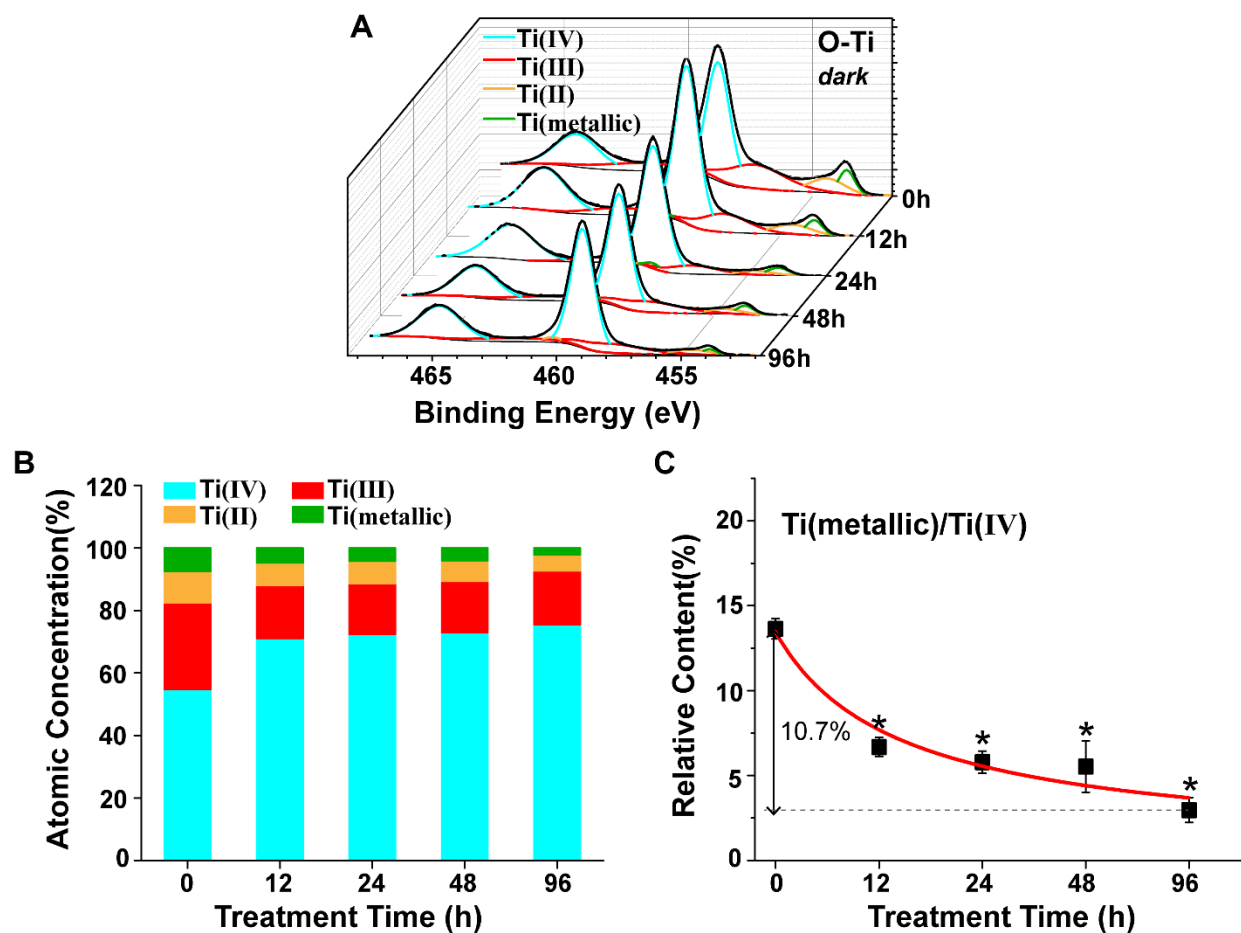
Acknowledgments We gratefully acknowledge Prof. Yong Wang (Department of Materials Science and Engineering, Zhejiang University), Prof. Hanying Li (Department of Polymer Science and Engineering, Zhejiang University), Prof. Yanwu Xie (Department of Physics, Zhejiang University), Prof. Kang Yu (Department of Pharmacy, Zhejiang University) and Prof. Huaiwen He (College of Law, Zhejiang University) for their support and useful discussions. Thank Senior engineer Ya Wang and for her help in FIB samples preparation. Thank Dr. Tulai Sun for his help in TEM study. This work was funded by the National key R&D program of China (2018YFC1105302 and 2018YFC1105304).

Author contributions X. L. conceived, designed and initiated this work; W. L., Q. L. carried out the experiments; Q. L., Y. H., C. L. and J. X. assisted X. L. and W. L. in analyzing the experiment data; H. Z. and X. W. performed the DFT calculations; X. D, X. L. and Q. C. participated in discussion; W. L. and Q. L. participated in writing and revising the manuscript; X. L. wrote, revised and finalized the manuscript.

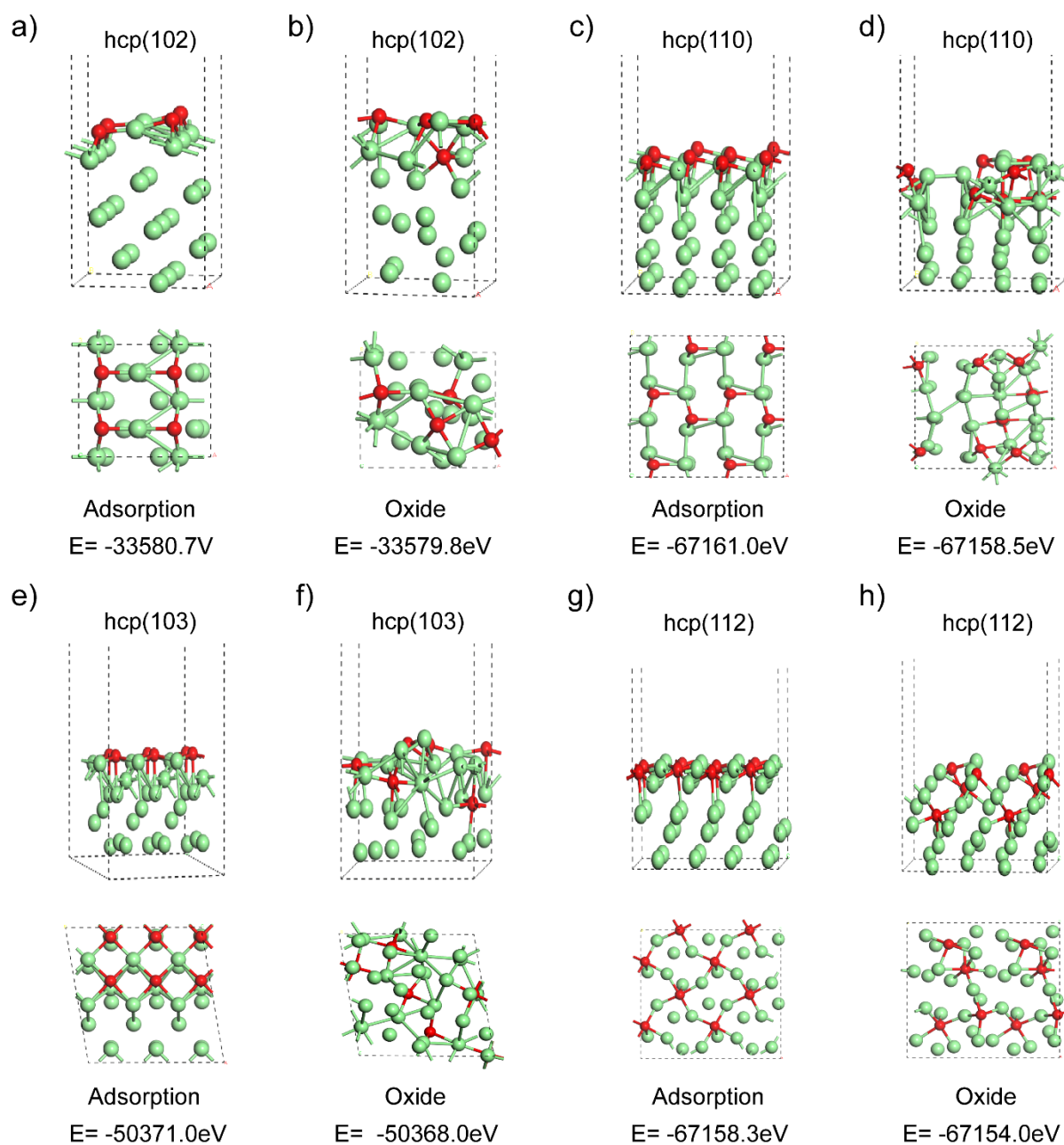
Competing interests Authors declare that they have no competing interests.



Extended Data Fig. 1. Deconvolution of Ti^{2p} peaks in XPS spectra on three Ti passivation films. (A) NA-Ti, (B) O₃-Ti, (C) O-Ti.

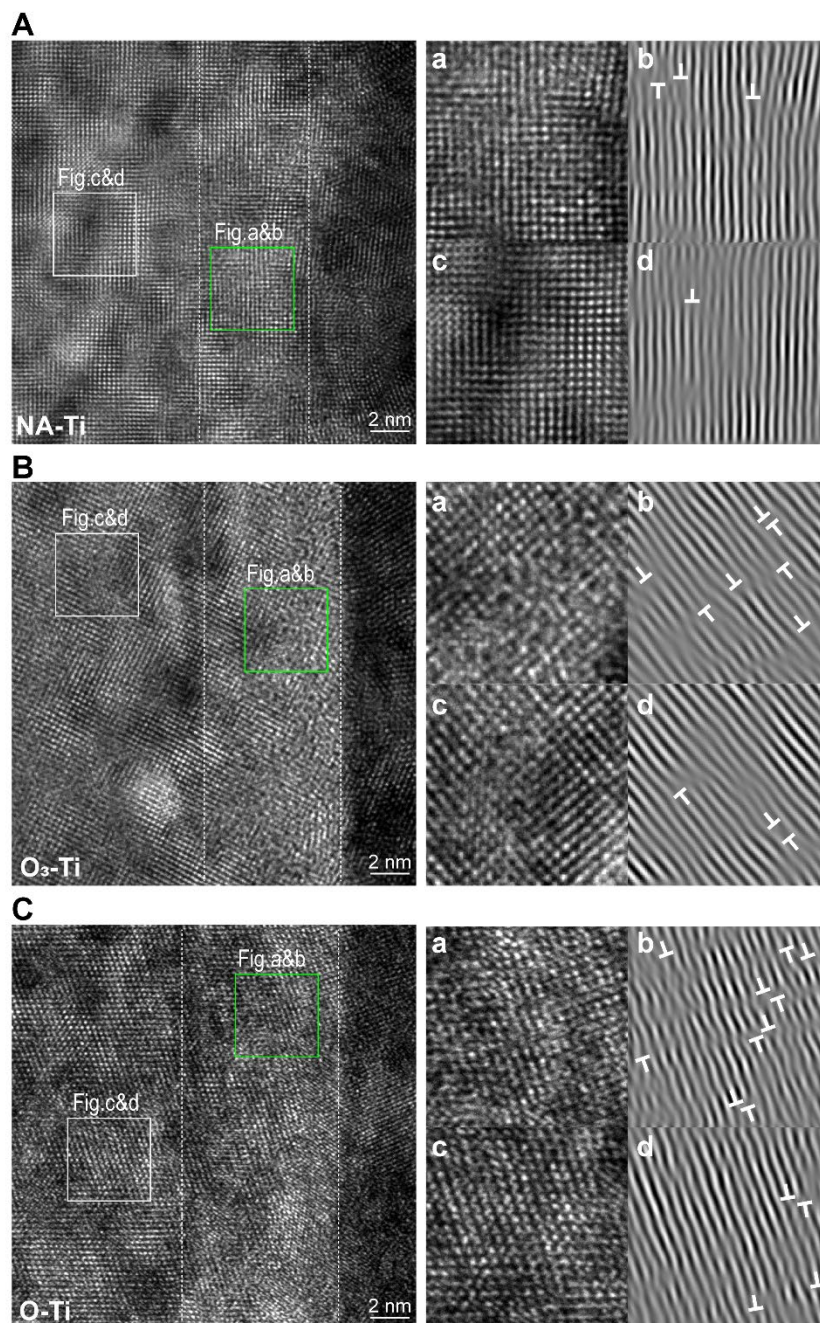


Extended Data Fig. 2. Elemental analysis of XPS spectra on O-Ti surfaces with UV irradiation under dark conditions. (A) Deconvolution of Ti^{2p} peaks. (B) Content percentage of various Ti valence states. (C) Trend charts of $\text{Ti}^{\text{metallic}}/\text{Ti}^{4+}$ relative content. $\text{Ti}^{\text{metallic}}$ content of O-Ti under dark conditions also significantly reduces from $7.47 \pm 0.43\%$ to $2.24 \pm 0.28\%$ along with Ti^{4+} increases from $54.75 \pm 0.77\%$ to $75.42 \pm 1.18\%$. * $p < 0.05$ vs. O-Ti *dark*-0h group.



Extended Data Fig. 3. A stable chemisorbed O-Ti atom monolayer on the outmost Ti surface. Chemisorption models of O atoms on different surfaces of hcp Ti as well as oxide models of TiO were constructed respectively. Side view and top view of chemisorption models of O atoms on hcp Ti (102) surface in a), (110) surface in c), (103) surface in e) and (112) surface in g). Side view and top view of Ti-O oxide models on hcp Ti (102) surface in b), (110)

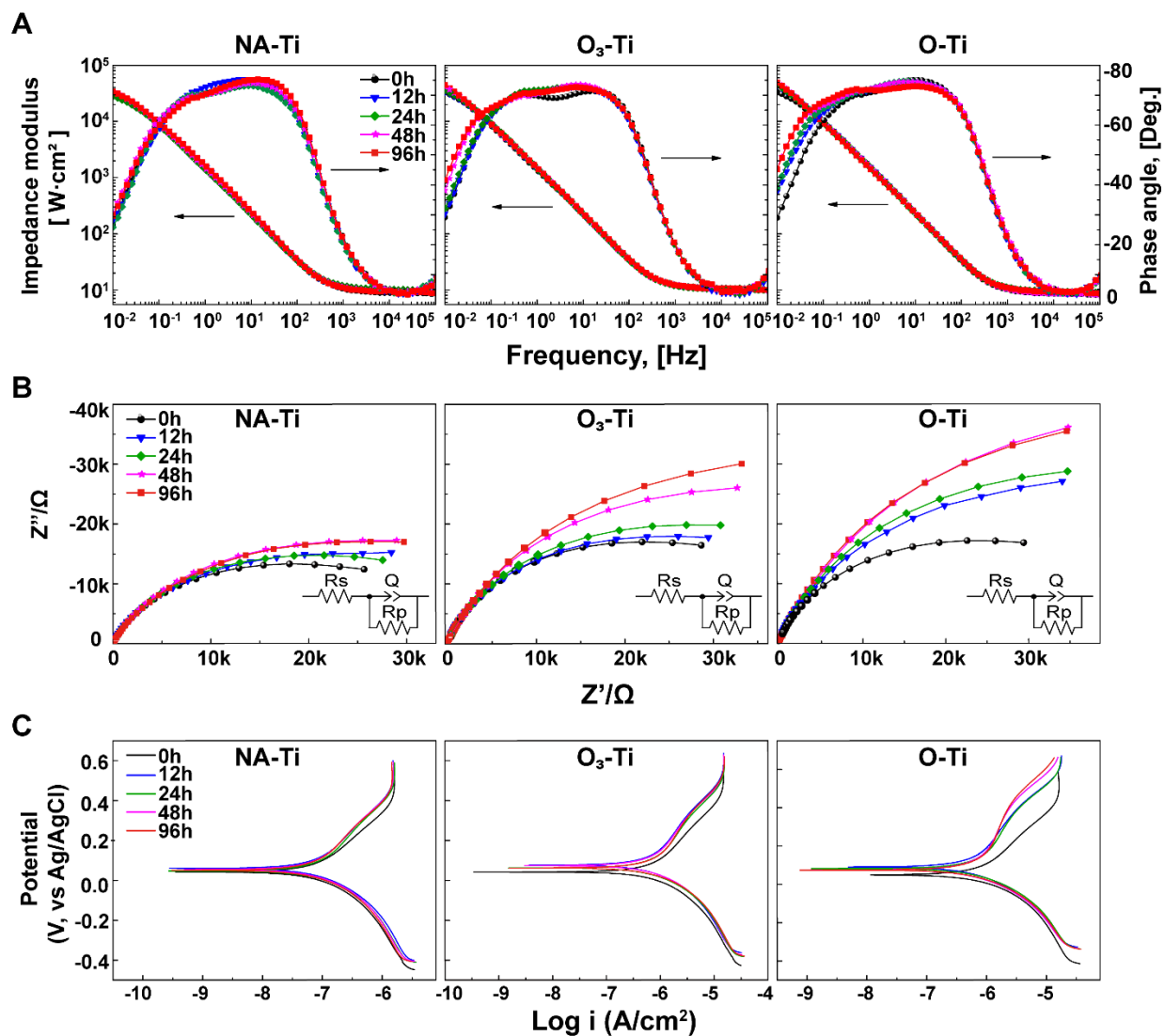
surface in d), (103) surface in f) and (112) surface in h). The simulated system has better stability with larger absolute value of energy (E). Take the energy at infinity from the nucleus as zero.



Extended Data Fig. 4. Micro-strains and O-vacancies analysis of the three Ti oxide layers.

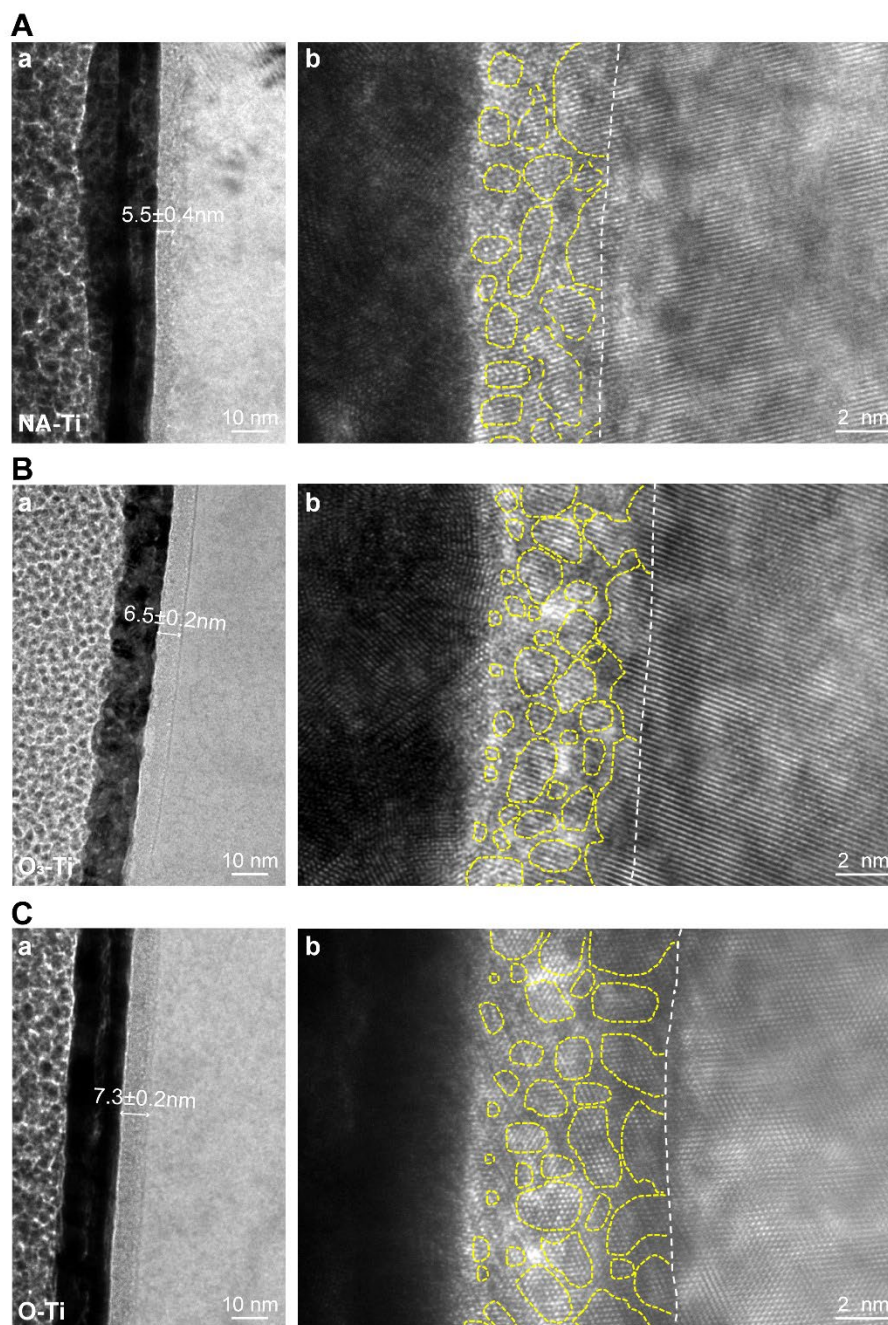
HRTEM images of NA-Ti (A), O₃-Ti (B) and O-Ti (C) with treatment for 48h. The number of edge dislocations from one-dimensional lattice fringe images (b, d) obtained by applying a fast

Fourier transform filtering process from oxide layer areas (Green box region a) and metal base areas (White box region c), respectively.



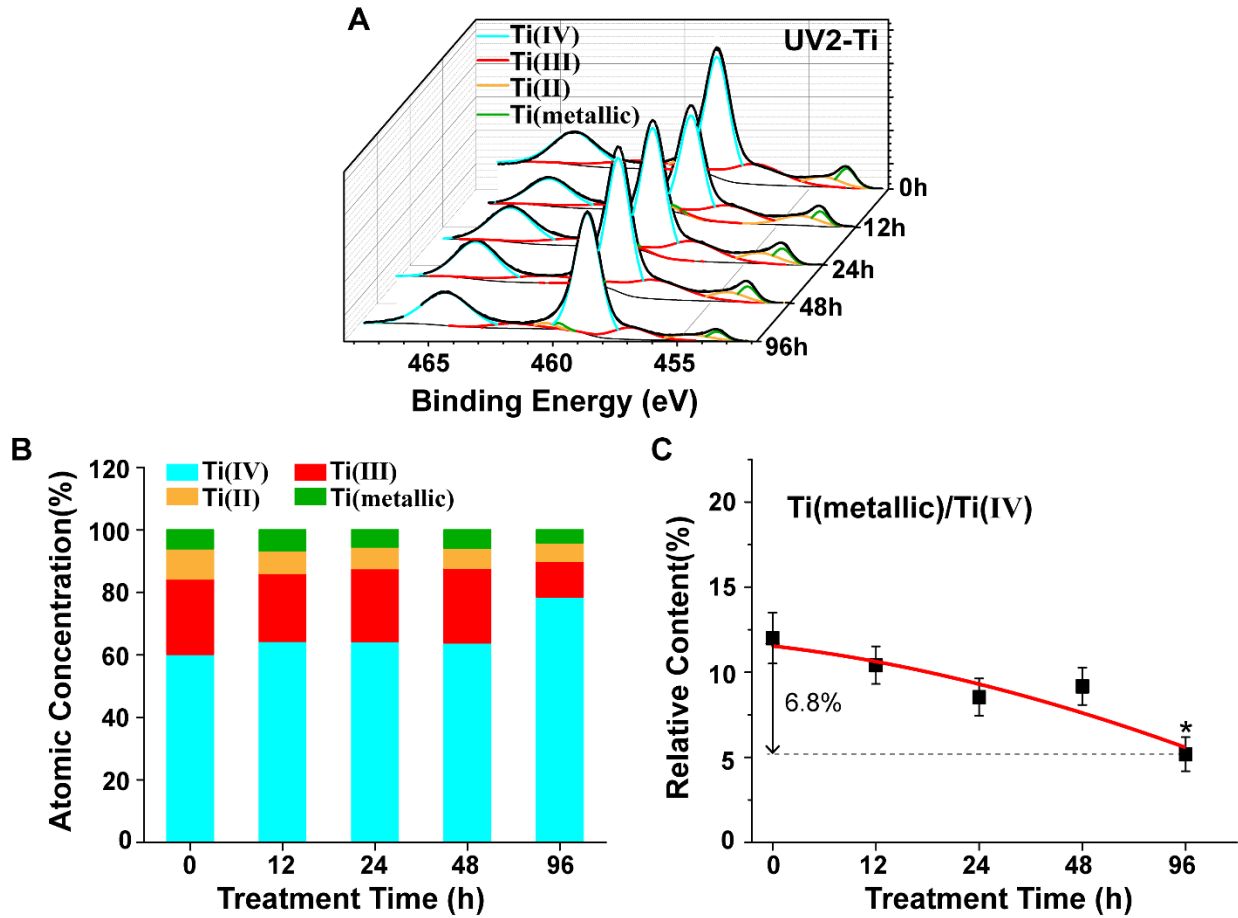
Extended Data Fig. 5. Electrochemical measurements of the three Ti surfaces. (A) Bode plots from EIS of NA-Ti, O₃-Ti and O-Ti. (B) Nyquist plots from EIS of NA-Ti, O₃-Ti and O-Ti. Inset is the equivalent circuit of film/solution interface. The impedance behavior of the passivation film can be described by the equivalent circuit of the film/solution interface, R_s (QR_p). In the equivalent circuit, R_s represents the resistance of solution; Q is the constant phase elements (CPE) used for describing the capacitance behaviors of the compact passivation film

and R_p is the polarization resistance. (C) Potentiodynamic polarization curves of NA-Ti, O₃-Ti and O-Ti.



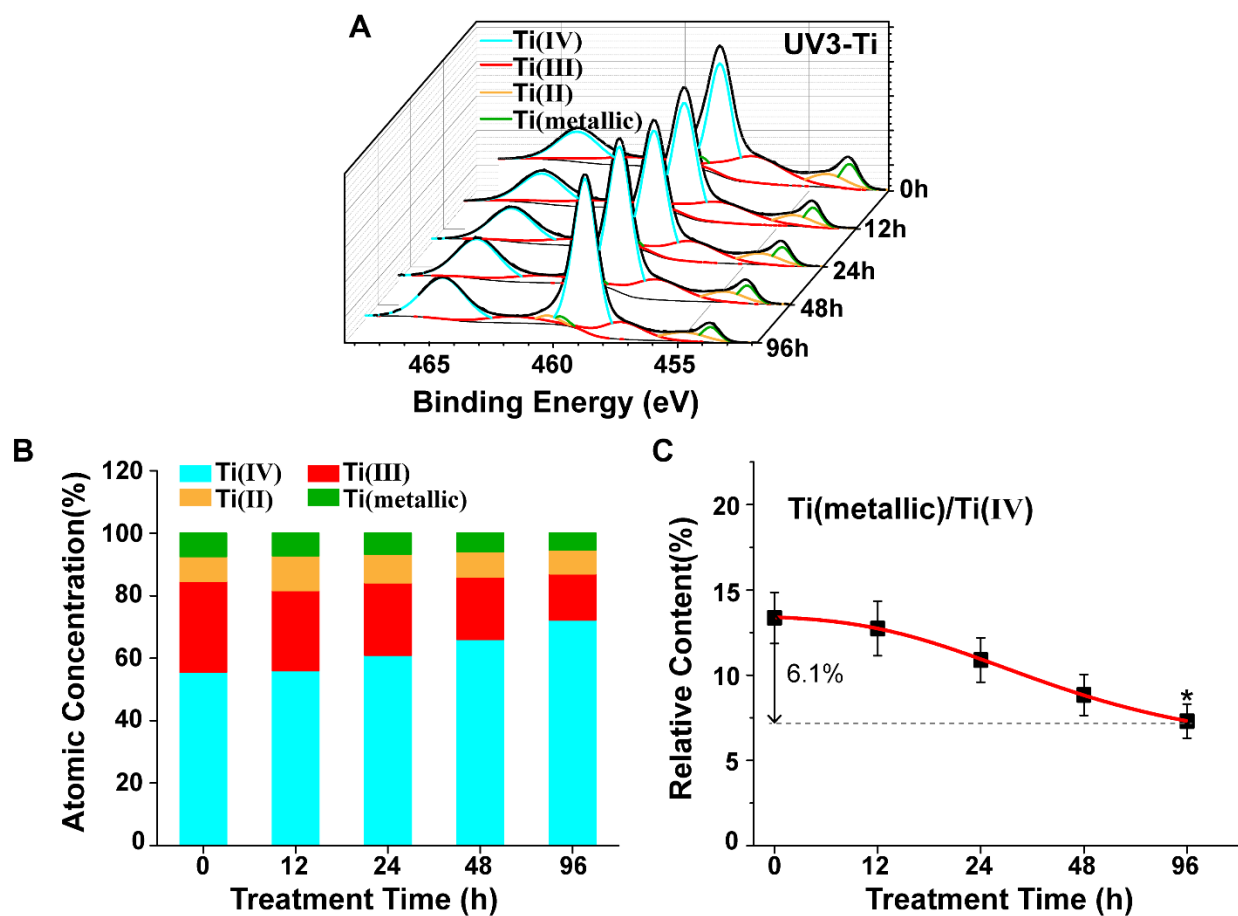
Extended Data Fig. 6. Oxide layers of a stone-wall like structure of the three Ti oxide layers. The oxide layers on O-Ti and O₃-Ti are thicker than that on NA-Ti with treatment for 48h [A(a), B(a) and C(a)]. Under room temperature atmosphere, Ti passivation film shows a gradient

heterogeneous stone-wall like structure of high entropy [A(b)]. Some residual Ti lattice structures are seen as stone in the passivation film. Under stronger oxidizing environment (O_3 or O), thicker passivation films with more stone-wall boundaries are induced to protect the internal matrix from stronger oxidation [B(b) and C(b)].



Extended Data Fig. 7. Elemental analysis of XPS spectra on surfaces of UV2-Ti. (A)

Deconvolution of Ti^{2p} peaks. (B) Content percentage of various Ti valence states. (C) Trend charts of $Ti^{metallic}/Ti^{4+}$ relative content. $Ti^{metallic}$ content just slowly weakens from $7.13 \pm 0.31\%$ to $4.08 \pm 0.2\%$ along with Ti^{4+} increases from $59.13 \pm 0.79\%$ to $78.63 \pm 0.71\%$. UV2-Ti is treated with the central wavelength of $254 \pm 20nm$ ($2.5mW/cm^2$). * $p < 0.05$ vs. UV2-Ti-0h group.



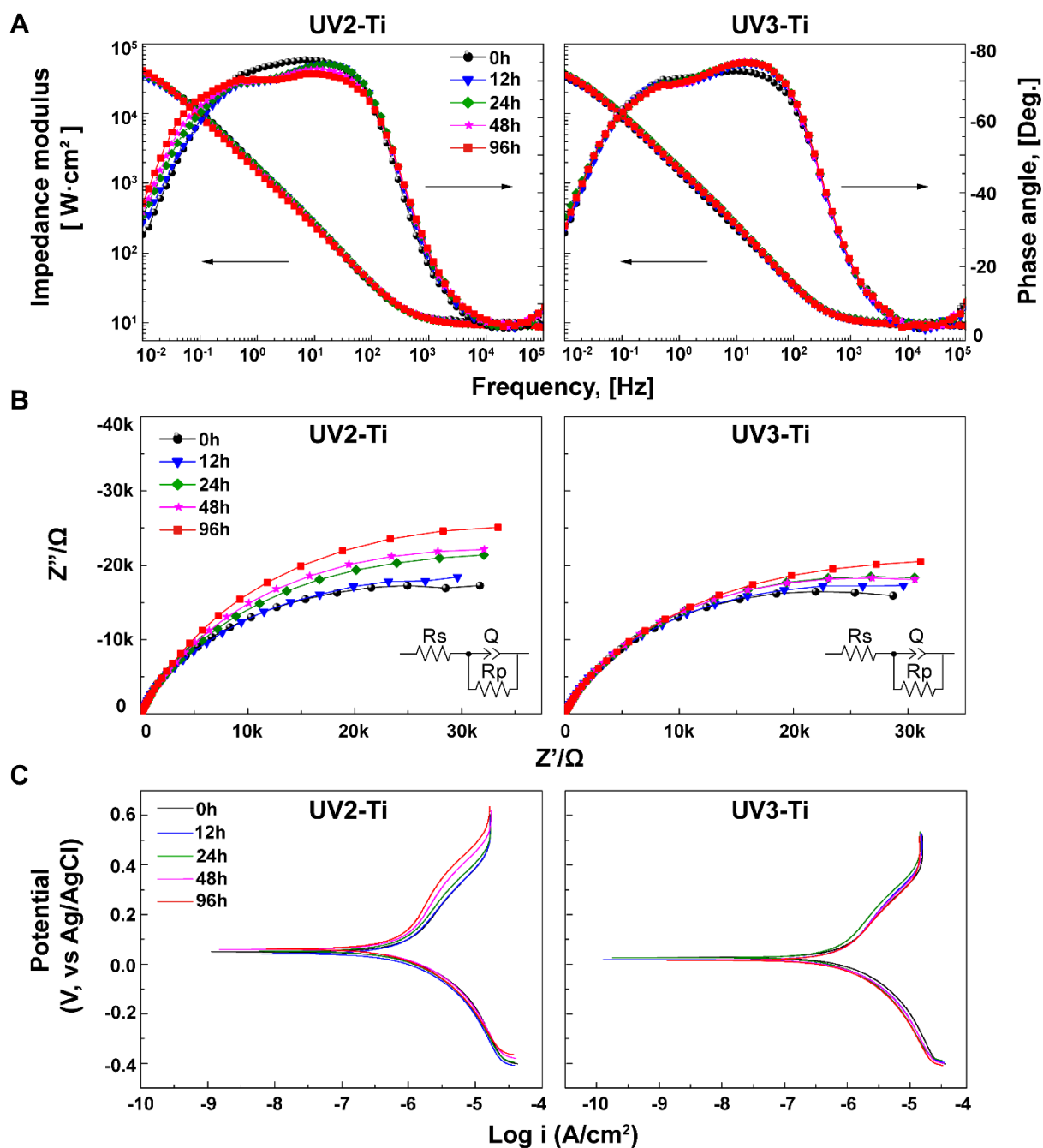
Extended Data Fig. 8. Elemental analysis of XPS spectra on surfaces of UV3-Ti. (A)

Deconvolution of Ti^{2p} peaks. (B) Content percentage of various Ti valence states. (C) Trend

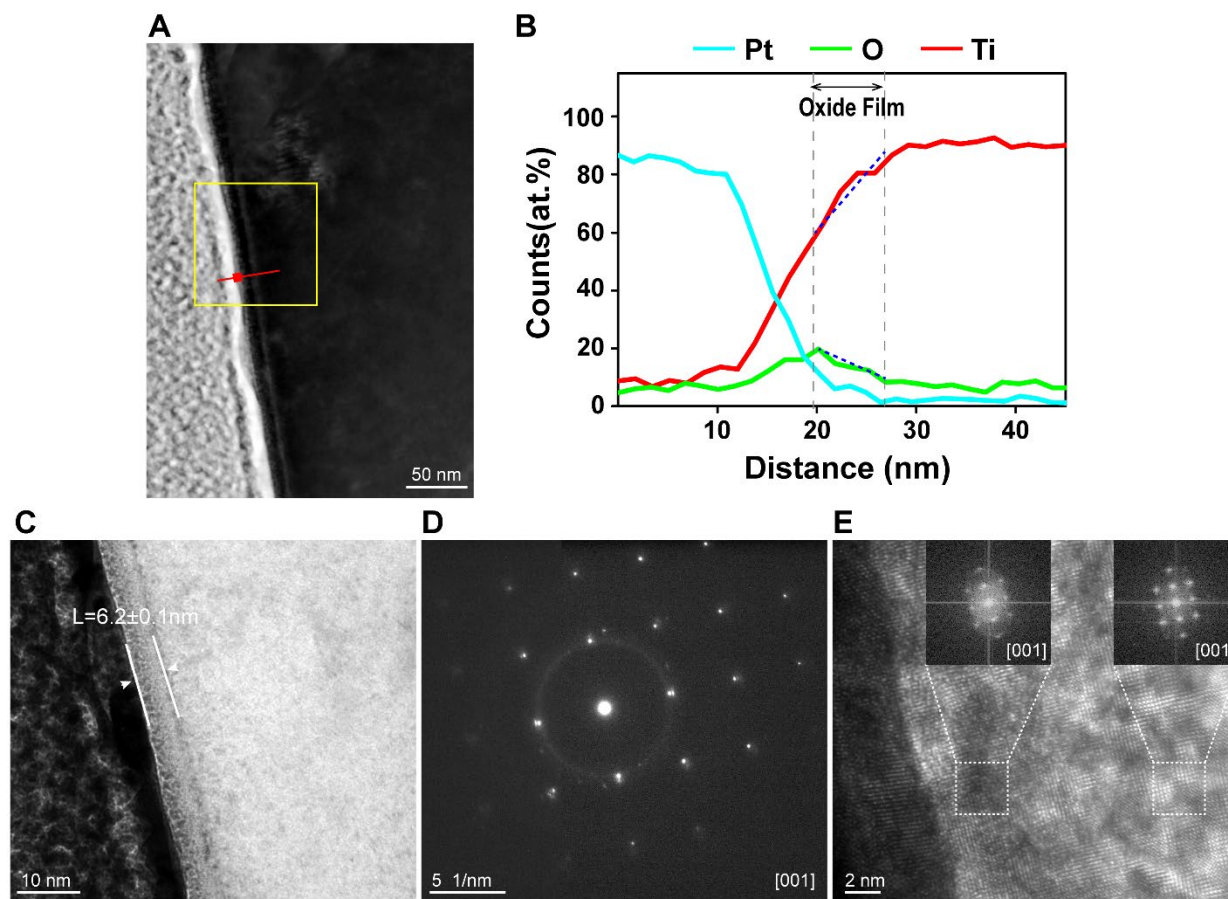
charts of $\text{Ti}^{\text{metallic}}/\text{Ti}^{4+}$ relative content. $\text{Ti}^{\text{metallic}}$ content reduces from $7.42 \pm 0.28\%$ to $5.28 \pm 0.21\%$

along with Ti^{4+} increases from $55.53 \pm 0.74\%$ to $72.28 \pm 0.63\%$. UV3-Ti is treated with the

central wavelength of $365 \pm 20\text{nm}$ ($2.4\text{mW}/\text{cm}^2$). * $p < 0.05$ vs. UV3-Ti-0h group.

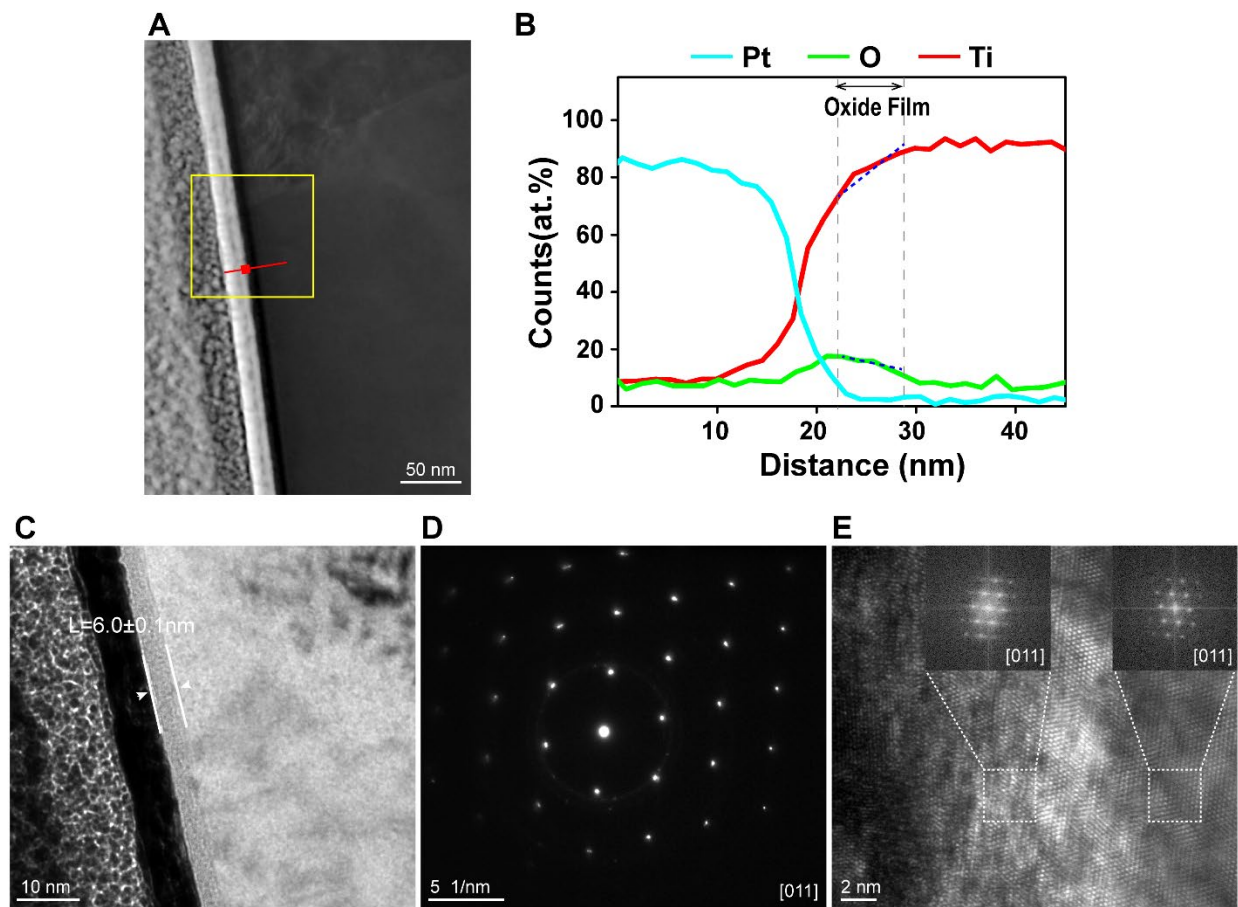


Extended Data Fig. 9. Electrochemical measurements of UV2-Ti and UV3-Ti. (A) Bode plots from EIS of UV2-Ti and UV3-Ti. (B) Nyquist plots from EIS of UV2-Ti and UV3-Ti. (C) Potentiodynamic polarization curves of UV2-Ti and UV3-Ti. Both UV irradiations have little effect on the structure and properties of Ti passivation film, slightly stronger than NA-Ti group and much weaker than O_3 -Ti and O-Ti.



Extended Data Fig. 10. Cross-sectional HRTEM observation of UV2-Ti oxide film. (A)

HAADF scanning transmission electron microscopic (HAADF-STEM) image of the passivation film on UV2-Ti with treatment for 48h. (B) Line profiles of the concentration gradient of Ti, O and Pt signals across the interface zone. (C) The HRTEM image of UV2-Ti shows that the passivation film thickness is 6.2 ± 0.1 nm. (D) SAED patterns of UV2-Ti. (E) FFT patterns of the passivation film and metal matrix on UV2-Ti.



Extended Data Fig. 11. Cross-sectional HRTEM observation of UV3-Ti oxide film. (A)

HAADF scanning transmission electron microscopic (HAADF-STEM) image of the passivation film on UV3-Ti with treatment for 48h. (B) Line profiles of the concentration gradient of Ti, O and Pt signals across the interface zone. (C) The HRTEM image of UV3-Ti shows that the passivation film thickness is 6.0 ± 0.1 nm. (D) SAED patterns of UV3-Ti. (E) FFT patterns of the passivation film and metal matrix on UV3-Ti.

Extended Data Table. 1.

EIS parameters of different treated Ti samples

Groups	Treatment Time (h)	R_s (Ω cm ²)	Q (μ F cm ⁻²)	n	R_p (k Ω cm ²)	Chi squared
NA-Ti	0	9.82 \pm 0.14	148.70 \pm 0.90	0.85 \pm 0.01	35.00 \pm 0.67	2.22 $\times 10^{-3}$
	12	9.42 \pm 0.09	132.80 \pm 1.95	0.86 \pm 0.01	37.02 \pm 1.47	2.79 $\times 10^{-3}$
	24	8.60 \pm 0.18	147.13 \pm 2.48	0.85 \pm 0.02	37.46 \pm 1.43	2.21 $\times 10^{-3}$
	48	8.84 \pm 0.12	132.97 \pm 0.95	0.84 \pm 0.01	40.97 \pm 0.29	5.27 $\times 10^{-3}$
	96	9.17 \pm 0.44	143.77 \pm 1.80	0.84 \pm 0.01	43.51 \pm 0.84	3.43 $\times 10^{-3}$
O ₃ -Ti	0	9.60 \pm 0.32	154.60 \pm 3.61	0.83 \pm 0.02	44.23 \pm 2.06	3.68 $\times 10^{-3}$
	12	10.41 \pm 0.50	147.50 \pm 2.88	0.84 \pm 0.03	44.50 \pm 2.90	1.95 $\times 10^{-3}$
	24	10.31 \pm 0.37	146.57 \pm 1.72	0.85 \pm 0.02	47.62 \pm 2.96	2.37 $\times 10^{-3}$
	48	10.26 \pm 0.80	151.27 \pm 2.04	0.84 \pm 0.01	64.33 \pm 0.57	3.58 $\times 10^{-3}$
	96	9.93 \pm 0.74	150.33 \pm 2.00	0.82 \pm 0.01	74.56 \pm 1.88	3.28 $\times 10^{-3}$
O-Ti	0	8.27 \pm 0.23	140.73 \pm 1.21	0.84 \pm 0.02	41.93 \pm 1.68	3.58 $\times 10^{-3}$
	12	9.27 \pm 0.20	136.27 \pm 3.19	0.84 \pm 0.02	62.84 \pm 1.50	3.46 $\times 10^{-3}$
	24	8.86 \pm 0.13	139.70 \pm 2.20	0.83 \pm 0.03	67.49 \pm 1.56	3.04 $\times 10^{-3}$
	48	8.28 \pm 0.27	140.10 \pm 2.19	0.84 \pm 0.03	88.82 \pm 3.18	3.58 $\times 10^{-3}$
	96	8.84 \pm 0.21	146.97 \pm 2.34	0.83 \pm 0.02	92.53 \pm 1.74	3.08 $\times 10^{-3}$
UV2-Ti	0	10.04 \pm 0.20	121.47 \pm 0.95	0.87 \pm 0.01	41.65 \pm 1.62	2.77 $\times 10^{-3}$
	12	9.43 \pm 0.44	128.40 \pm 2.00	0.83 \pm 0.02	43.66 \pm 0.86	5.18 $\times 10^{-3}$
	24	9.36 \pm 0.24	130.97 \pm 3.02	0.85 \pm 0.04	52.01 \pm 1.56	4.66 $\times 10^{-3}$
	48	9.36 \pm 0.43	140.20 \pm 2.31	0.84 \pm 0.04	55.58 \pm 1.60	2.91 $\times 10^{-3}$
	96	8.91 \pm 0.38	147.80 \pm 1.49	0.83 \pm 0.03	65.65 \pm 1.90	2.24 $\times 10^{-3}$
UV3-Ti	0	8.78 \pm 0.48	151.67 \pm 3.00	0.82 \pm 0.01	42.35 \pm 2.18	2.66 $\times 10^{-3}$
	12	9.28 \pm 0.27	139.63 \pm 2.70	0.86 \pm 0.02	42.60 \pm 2.13	5.25 $\times 10^{-3}$
	24	9.17 \pm 0.34	137.23 \pm 2.02	0.83 \pm 0.02	45.28 \pm 3.02	5.96 $\times 10^{-3}$
	48	9.46 \pm 0.35	137.83 \pm 2.05	0.84 \pm 0.03	44.58 \pm 2.87	6.05 $\times 10^{-3}$
	96	9.40 \pm 0.34	132.33 \pm 4.09	0.84 \pm 0.01	47.58 \pm 2.24	6.22 $\times 10^{-3}$

Extended Data Table. 2.

Corrosion parameters of potentiodynamic polarization for different treated Ti samples in PBS solution at 37°C

Groups	Treatment Time (h)	$E_{\text{corr}}(\text{mV})$	$I_{\text{corr}} (\mu\text{A cm}^{-2})$
NA-Ti	0	101.41±1.53	1.26±0.06
	12	101.52±0.81	1.23±0.15
	24	103.72±1.33	1.22±0.20
	48	106.94±1.79	1.20±0.17
	96	107.83±0.76	1.18±0.04
O ₃ -Ti	0	112.12±0.47	1.28±0.04
	12	114.53±3.15	1.02±0.07
	24	119.65±2.43	0.89±0.03
	48	123.63±1.26	0.76±0.02
	96	129.63±0.55	0.70±0.05
O-Ti	0	127.65±1.96	1.51±0.09
	12	133.67±2.53	0.66±0.04
	24	139.53±1.24	0.64±0.05
	48	142.38±2.62	0.63±0.03
	96	149.62±1.21	0.60±0.01
UV2-Ti	0	98.26±1.00	1.10±0.24
	12	98.57±1.59	1.06±0.05
	24	99.93±0.40	1.02±0.04
	48	102.44±1.54	0.99±0.05
	96	105.35±2.03	0.94±0.10
UV3-Ti	0	110.82±1.92	1.12±0.07
	12	111.01±3.26	1.11±0.08
	24	113.73±2.84	1.08±0.12
	48	115.96±2.18	1.05±0.10
	96	117.84±3.02	1.00±0.10